Journal of
Materials Chemistry A

ROYAL SOCIETY
OF CHEMISTRY

PAPER

Cite this: *J. Mater. Chem. A*, 2024, **12**, 22013

In-depth understanding of electrochemical energy storage efficiency in a series of new 3d–4d mixed metal polyoxometalates: experimental and theoretical investigations†

Kalyankumar S. Morla,[a] Dewendra Thakre,[a] Tushar Balasaheb Deshmukh, [b] Sunanda Malo, [c] Subuhan Ahamed,[c] Ravari Kandy Aparna,[d] Subham Sahoo, [e] Debajit Sarma, [e] Kartik Chandra Mondal, [c] Babasaheb R. Sankapal *[b] and Abhishek Banerjee *[a]

Transition-metal complexes, with their reversible redox properties, are the basis for electrochemical energy storage devices, such as rechargeable batteries and supercapacitors. In order to comprehend the variation in the electronic properties and electrochemical activity of concurrent transition elements existing in identical coordination environments, we have pursued extensive multi-method spectroscopic and electrochemical studies of three new isostructural 3d–4d mixed metal polyoxometalate complexes, *viz.* the vanado-molybdate $Na_2(NH_4)_5[(Mo^{VI}_2O_5)_2(V^{III}O_2)\{O_3P\text{-}C(O)(CH_2\text{-}4\text{-}C_5NH_4)\text{-}PO_3\}_2]\cdot 10H_2O$ (**1a**), the chromo-molybdate $(NH_4)_5[H_2(Mo^{VI}_2O_5)_2(Cr^{III}O_2)\{O_3P\text{-}C(O)(CH_2\text{-}4\text{-}C_5NH_4)\text{-}PO_3\}_2]\cdot 10H_2O$ (**2a**) and the mangano-molybdate $Na(NH_4)_6[H(Mo^{VI}_2O_5)_2(Mn^{III}O_2)\{O_3P\text{-}C(O)(CH_2\text{-}4\text{-}C_5NH_4)\text{-}PO_3\}_2]\cdot 9H_2O$ (**3a**). The structures of the polyanions have been determined using single-crystal X-ray diffraction studies, with all three polyanionic complexes having identical connectivity and arrangement in the solid state. The electronic properties of the complexes have been analyzed thoroughly with electronic paramagnetic resonance (EPR) and X-ray photoelectron spectroscopy (XPS) methods. EPR measurements for all three complexes are characterized by $\Delta m_s = \pm 2$ signals (forbidden half-field transition) at 77 K in the solid state, confirming the existence of V^{III}, $S = 1$ for **1a**; Cr^{III}, $S = 3/2$ for **2a**; Mn^{III}, $S = 2$ for **3a**. Using our original and novel binder-free approach to prepare supercapacitor electrodes, thorough comparative electrochemical energy storage studies have been performed on the three compounds using cyclic voltammetry, galvanostatic charge–discharge, electrochemical impedance spectroscopy, and cycling stability tests. The oxo-vanado-molybdate complex has shown superior electrochemical performance, with respect to specific capacitances, energy density, power density, and electrochemical stability, followed by the oxo-chromo-molybdate and the oxo-mangano-molybdate complexes. The electrochemical performance trend has been corroborated by DFT calculations at the B3LYP-D3(BJ)/Def2-SVP level of theory in a polar medium, with the same order of promptness of undergoing oxidation of the polyanionic species [M^{2+} to M^{3+}; M = V (**1′**) > Cr (**2′**) > Mn (**3′**); $\Delta G(M^{3+}\text{–}M^{2+})$ = +48 (**1′**), +58 (**2′**), +81 (**3′**) kcal mol^{-1}], corroborating the experimental observations. The oxidation of these anionic species from 8-(M^{II}) to 7-(M^{III}) has thus been computed to be highly favourable in the gas phase [∼−328 (**1′**), −311 (**2′**), and −309 (**3′**) kcal mol^{-1}]. The studies on the HOMO–LUMO structures of the complexes also corroborate the trend of the electrochemical behavior.

Received 7th May 2024
Accepted 12th July 2024

DOI: 10.1039/d4ta03188a

rsc.li/materials-a

---

[a] *Department of Chemistry, Visvesvaraya National Institute of Technology, Nagpur, India. E-mail: abhishekbanerjee@chm.vnit.ac.in*

[b] *Department of Physics, Visvesvaraya National Institute of Technology, Nagpur, India. E-mail: brsankapal@gmail.com*

[c] *Department of Chemistry, Indian Institute of Technology Madras, Chennai, India*

[d] *Department of Chemistry, Indian Institute of Science Education and Research Thiruvananthapuram, Thiruvananthapuram, India*

[e] *Department of Chemistry, Indian Institute of Technology Patna, Patna, India*

† Electronic supplementary information (ESI) available. CCDC 2345425–2345427. For ESI and crystallographic data in CIF or other electronic format see DOI: **https://doi.org/10.1039/d4ta03188a**

1. Introduction

Electrochemical energy storage devices have been the backbone of modern electronics and the accompanying age of portable electronics.[1–3] The most important types of electrochemical storage devices come in two forms, batteries and capacitors, which function in fundamentally different ways.[4–6] While batteries store energy through chemical reactions where the stored chemical energy is converted to electrical energy *via* reactions releasing electrons, which flow through an external circuit to provide electrical energy, *i.e.* discharging,[7] capacitors store energy in an electric field created between two metal plates (electrodes), with an insulating material (dielectric) in between, with no chemical reaction being involved in the energy storage process.[8–10] As such, batteries generally have high energy density, and capacitors on the other hand have high power density. This makes batteries suitable for applications where long-lasting energy is needed,[11–13] while capacitors are ideal for applications that require immediate power supply for a short duration. Batteries and capacitors therefore form the two extreme ends of energy *vs.* power density. Supercapacitors bridge this gap, offering higher power density than the former and higher energy density than the latter.[14,15]

A supercapacitor, also known as an ultracapacitor or double-layer capacitor, is a type of capacitor that has a very high capacitance compared to standard capacitors. Since supercapacitors offer amazing qualities like high specific capacitance, higher power density, and long-term stability, they have become a better prospect for the future,[16–19] and are used in applications where rapid charging and discharging of energy are required. Unlike batteries, which rely on chemical reactions, supercapacitors store and release energy through a physical process, involving the separation of charge at the interface between an electrode and an electrolyte.[20,21] This process occurs in the electric double layers formed at the surfaces of the electrodes. As such supercapacitors can be classified according to their mechanism of energy storage: electrochemical double layer capacitance (EDLC) and pseudocapacitance.[22] While in EDLC there is an electrostatic separation of charges at the interface between an electrode and an electrolyte solution, pseudo-capacitance involves faradaic redox reactions at the electrode–electrolyte interface.[23] This means that during charge and discharge cycles in EDLC-type supercapacitors, no faradaic redox reactions occur; instead, charges accumulate at the electrode–electrolyte interface in the form of an electric double layer,[24] while in pseudo-capacitors reversible electrochemical reactions occur within the bulk of the electrode material.[25] Materials that show a combination of the two properties, *vis á vis* hybrid supercapacitors,[26–30] therefore show superior performance.

The choice of electrode material(s) is of paramount importance in the building of a hybrid supercapacitor with high efficiency.[31,32] EDLC materials primarily consist of carbon-based substances like activated carbon, MWCNTs, *etc.*,[33–35] whereas different metal oxides like V_2O_5, MoO_3, MnO_2,WO_3, *etc.*, are involved in pseudocapacitance.[36–40] However, the low power, low energy density, and poor rate performance encountered with these materials still leave numerous issues. Therefore, in order to improve supercapacitive performance, it is imperative to look into materials with multifunctional behaviour. In this respect, polyoxometalates (POMs) have great potential to act as efficient electrode materials, and their exploration has led to new developments in this field.[41–43] POMs exhibit unique properties, such as versatile redox activity, tuneable electronic properties and fast electron transfer capacity due to redox activity.[44] The stable and compatible nature of these materials makes them effective and promising candidates for energy storage applications.[45,46] The multielectron transmitting features of POMs with different oxidation states possessed by metal cations enable them to be effective materials for studying pseudocapacitance.[47,48] In combination with carbonaceous materials, such as activated carbon, carbon nanotubes, *etc.*, these materials have shown great promise towards the fabrication of hybrid-type supercapacitor electrodes.[49,50] Nevertheless, certain limiting properties such as solubility, low surface area, and weak adherence to an electrode limit their practical usage in aqueous electrolyte solutions.[51,52] To overcome such shortcomings, researchers have focused on the POM materials' design, structure, composition, and fabrication. The formation of composites with the integration of POMs with carbon-based materials, conducting polymers, and metal–organic frameworks, to provide better adherence power between the material and electrode surface with the use of various binders such as PVDF, MES, *etc.*, can eventually improve insolubility character in the electrolyte solution,[53–55] but at the cost of electrochemical efficiency. Numerous research teams have therefore continued work on such a combination of materials with a great variety of POM compounds. In this respect, our team has developed a novel binder-free approach towards the fabrication of supercapacitor electrodes, using sustainable growth of particle films with simple solvent evaporation techniques.

Our group has been primarily interested in the study of organic–inorganic hybrid diphosphonate-functionalized POMs, a subclass within the hybrid-POM literature, towards energy storage applications.[56] The presence of diphosphonate ligands makes such compounds adopt a more open-type assembly, as compared with classical POM structures. In the case of polyoxovanadates, this leads to the presence of varied oxidation states and coordination environments of the same metal atom, *viz.* vanadium, within the structure.[57,58] Such versatility makes these complexes extremely interesting for electrochemical applications.

In order to gain a better understanding of redox processes involved in different metal atoms in identical environments, which eventually influence their electrochemical efficiency(ies), we have strived to study isostructural complexes with different transition metals, wherein except for the metal itself, the rest of the parameters such as the coordination environment and the oxidation state of the metal(s) remain the same. Our focus has always been to compare the redox efficiency of vanadates against other 3d-transition metal complexes. Since it proved difficult to synthesize iso-structural vanadate complexes with other 3d-metal ions, we endeavoured to explore a mixed-metal

3d–4d system. As such, we have been successful in synthesizing three new isostructural compounds with the formulae $Na_2(NH_4)_5[(Mo^{VI}_2O_5)_2(V^{III}O_2)\{O_3PC(O)(CH_2\text{-}4\text{-}C_5NH_4)PO_3\}_2]\cdot 10H_2O$ (**1a**), $(NH_4)_5[H_2(Mo^{VI}_2O_5)_2(Cr^{III}O_2)\{O_3P\text{-}C(O)(CH_2\text{-}4\text{-}C_5H_4N)\text{-}PO_3\}_2]\cdot 10H_2O$ (**2a**) and $Na_1(NH_4)_6[H(Mo^{VI}_2O_5)_2(Mn^{III}O_2)\{O_3P\text{-}C(O)(CH_2\text{-}4\text{-}C_5H_4N)\text{-}PO_3\}_2]\cdot 9H_2O$ (**3a**), in a one pot reaction. All three compounds have isostructural polyanionic units, formulated as $[(Mo^{VI}_2O_5)_2(MO_2)\{O_3PC(O)(CH_2\text{-}4\text{-}C_5NH_4)PO_3\}_2]^{7-}$, where M = V(III), Cr(III) and Mn(III) for polyanions **1**, **2** and **3**, respectively, and even crystallize in an identical space group. The structures of the compounds were obtained using the single-crystal X-ray diffraction method, and the oxidation state of the metal ion(s) was determined using bond-valence-sum (BVS) calculations and corroborated by several spectroscopic methods. With the central 3d-metal atom(s) vanadium, chromium and manganese in the three polyanions **1–3** possessing identical charge and coordination environment, this makes them excellent candidates for a thorough comparative analysis, with respect to their electronic and electrochemical properties. We have therefore aimed to correlate the electronic states of d-orbitals in central hetero-metal atoms using DFT studies and their effect on the electrochemical behavior of the complexes **1–3**. Using our already optimized binder-free approach for making supercapacitor electrodes with multi-walled carbon nanotubes (MWCNTs), extensive electrochemical analyses, such as cyclic voltammetry (CV), galvanostatic charge–discharge (GCD), electrochemical impedance spectroscopy (EIS), and cycling stability tests using a three-electrode system on the electrochemical workstation, have been performed. Synergistic effects between the pseudocapacitive material(s), *i.e.* complexes **1a–3a**, and the electrochemical double layer capacitive (EDLC) material MWCNTs result in the electrodes displaying hybrid characteristics and acting as hybrid electrode(s) with enhanced supercapacitive performance. A thorough comparative analysis of the electrochemical properties such as specific capacitance, energy density, power density, *b*-values, surface contribution, resistive components, and cycling stability, for complexes **1a**, **2a**, and **3a**, provides us with a greater insight into their electronic properties.

2. Experimental section

2.1 Materials and methods

Chemicals used for organic ligand synthesis, metal salts and electrolytic materials were procured from commercial sources and used without purification. Millipore water was used for the synthesis of the compounds **1a**, **2a**, and **3a**.

Powder X-ray diffraction (P-XRD) data were collected at room temperature on a Bruker D8ECO with a Cu-K_α radiation source ($\lambda = 0.154$ nm) in an angular range of 5–90° 2θ. Infrared spectra were recorded in transmittance mode on a Thermo Fisher Scientific iS50 spectrometer in the mid-IR region (4000–400 cm^{-1}) at room temperature. The X-band EPR spectra were recorded with a JEOL JES-FA series at 9.45 GHz, and all complexes **1a–3a** were measured in solid and solution phases. Elemental analysis for C, H, N, and O was performed on a Thermo Scientific Flash 2000 Organic Elemental Analyzer (CHNS/O Mode). Elemental analysis for Mo, V, Cr, Mn and P was performed using a quadrupole inductively coupled plasma-mass spectrometer (ICP-MS, Thermo X Series II). FESEM analysis was done on an ULTRA55 FE-SEM Karl Zeiss MonoCl integrated with an EDX analyser, and XPS analysis was done on an Omicron Nanotech instrument with MgKα (1253.6 eV) radiation. Electrochemical analysis was performed on a PARSTAT 4000 potentiostat/galvanostat (Princeton Applied Research) electrochemical workstation at room temperature. All the electrochemical analyses were carried out in a ternary solvent mixture of ethylene carbonate, propylene carbonate, and ethyl acetate in a volume ratio of 1 : 1 : 1, containing 0.5 M $NaClO_4$. This is referred to as 0.5 M $NaClO_4$ electrolyte solution.

2.1.1 Single-crystal X-ray diffraction. Data on single crystals of **1a** and **2a** were obtained on a BRUKER AXS (D8 Quest System) X-ray diffractometer equipped with a PHOTON 100 CMOS detector using Mo Kα radiation ($\lambda = 0.71073$ Å), at 293(2) K. Routine Lorentz and polarization corrections were applied, and absorption correction was performed using the SADABS program. Data on a single crystal of compound **3a** were collected at 180 K on a Stoe STADIVARI diffractometer (Ga-Kα = 1.34143 Å and detector: Dectris Eiger2 R 4M). Absorption corrections were applied using LANA.[59] Direct methods were used to solve the structures and to locate the heavy atoms (SHELXS97), and the remaining atoms were found from successive difference maps (SHELXL-2018).[60] The hydrogens of all the C atoms were added in calculated positions and refined using a riding model. Crystallographic data are summarized in Table 1. CCDC 2345425–2345427 contains the ESI† crystallographic data for this paper.

2.1.2 $[Mo^{V}_2O_4(H_2O)_6]^{2+}$. The synthesis of the dimeric unit of molybdenum $[Mo^{V}_2O_4(H_2O)_6]^{2+}$ was performed according to a literature procedure.[61] To a suspension of Na_2MoO_4 (4 g, 3.2 mmol) in 4 M hydrochloric acid solution (80 mL), $N_2H_4\cdot 3H_2O$ (210 μL, 4.29 mmol) was added. The colour of the solution changed slowly from yellow to dark red during heating at 80 °C for 3 h. The solution was then allowed to cool to room temperature and used for further reactions.

2.1.3 1-Hydroxo-2-(4-pyridyl) ethylidene-1,1-bisphosphonic acid. 1-Hydroxo-2-(4-pyridyl) ethylidene-1,1-bisphosphonic acid was synthesized according to the literature[62] and characterized using NMR spectroscopy. To 2.0 g (11.5 mmol) of 4-pyridyl acetic acid hydrochloride, taken in a 100 mL two-necked flask equipped with a reflux condenser, 3.6 g (43.8 mmol) of phosphorus acid and 12 g (86.3 mmol) of *p*-nitrophenol were added. This mixture was heated to 90 °C for a period of approximately 2 h until all of the solids had melted to form a homogeneous mixture and a thick suspension. Then 7.0 g of phosphorus trichloride was added to this suspension, and the resulting mixture was kept at 90 °C for an additional period of 6 h, after which a yellow, gel-like material was obtained. This mixture was allowed to cool to room temperature. 20 mL of water was then added dropwise, and the mixture was refluxed for 12 h. Then the mixture was again allowed to cool to room temperature. 20 mL of methanol was then added, and the precipitated product was stirred at 0–5 °C for an additional period of 2 h. A white, amorphous product was obtained by filtration and washed with

Table 1 Crystal data and structure refinement parameters of the complexes **1a**, **2a**, and **3a**

Complex	**1a**	**2a**	**3a**
Empirical formula	$Na_2VMo_4P_4C_{14}N_7O_{36}H_{52}$	$CrMo_4P_4C_{14}N_7O_{36}H_{54}$	$NaMnMo_4P_4C_{14}N_8O_{36}H_{56}$
Molar mass (g mol^{-1})	1499.18	1456.28	1498.23
Crystal system	Monoclinic	Monoclinic	Monoclinic
Space group	$P2_1/n$	$P2_1/n$	$P2_1/n$
a (Å)	12.3234(7)	12.494(2)	12.4413(3)
b (Å)	10.5882(6)	10.9438(18)	11.0036(3)
c (Å)	17.3903(11)	16.817(3)	17.3237(5)
α (°)	90	90	90
β (°)	99.099(2)	99.339(4)	100.425(2)
γ (°)	90	90	90
Volume (Å^3)	2240.6(2)	2269.0(7)	2332.45(11)
Z	2	2	2
Temp (K)	298(2)	298(2)	180(2)
D_{calcd} (g cm^{-3})	2.222	2.132	2.133
Abs coeff (μ mm^{-1})	1.569	1.562	8.855
F(000)	1492	1454	1496
Crystal size (mm)	0.48 × 0.33 × 0.21	0.46 × 0.23 × 0.15	0.10 × 0.10 × 0.03
Theta range for data collection (°)	2.550–26.118	2.455–28.397	3.522–62.512
R(int)	0.0576	0.0381	0.0244
T_{min}/T_{max}	0.520/0.734	0.534/0.799	0.471/0.777
GoF	1.052	1.114	1.071
$R1$ [$I > 2\sigma(I)$]	0.0532	0.0342	0.0495
$wR2^a$	0.1430	0.0986	0.1350

^{a} $R1 = \Sigma||F_o| - |F_c||/\Sigma|F_o|$. $wR2 = \{\Sigma[w(F_o^2 - F_c^2)]/\Sigma[w(F_o^2)^2]\}s^{1/2}$.

methanol (yield 2.271 g, 69.6%). ^{1}H NMR (500 MHz, D_2O/NH_3): δ (ppm) 3.156 (t, $^3J_{H-P} = 12.5$ Hz, 2H), 7.391 (d, $^2J_{H-H} = 6$ Hz, 2H), 8.259 (d, $^2J_{H-H} = 6$ Hz, 2H). ^{31}P NMR (500 MHz, D_2O/NH_3): δ (ppm) 17.2.

2.1.4 $\mathbf{Na_2(NH_4)_5[(Mo_2^{VI}O_5)_2(V^{III}O_2)\{O_3P\text{-}C(O)(CH_2\text{-}4\text{-}C_5NH_4)\text{-}PO_3\}_2]\cdot 10H_2O}$ (1a). To 20 mL of $[Mo_2^VO_4(H_2O)_6]^{2+}$ solution (2 mmol) in 4 M HCl, 0.1225 g of $NaVO_3$ (1 mmol) was added and the pH was adjusted to 1.50 using concentrated ammonia solution. Following this, 0.60 g of 1-hydroxo-2-(4-pyridyl) ethylidene-1,1-bisphosphonic acid (2 mmol) was added, and the final pH was increased and maintained at 7.80 by the further addition of concentrated ammonia solution. The solution mixture was kept for heating at 80 °C for one hour, and then the solution was allowed to cool to room temperature and filtered. The resulting solution was left for slow evaporation for two days, yielding dark brown coloured block-shaped crystals of **1a**. Yield: 0.36 g (24% based on vanadium). Elemental analysis (%) calculated for **1a**: Na: 3.07, Mo: 25.60, V: 3.40, P: 8.26, C: 11.22, H: 3.50, N: 6.54, O: 38.42. Found: Na: 2.87, Mo: 25.41, V: 3.51, P: 8.53, C: 11.50, H: 3.44, N: 7.12, O: 38.24.

2.1.5 $\mathbf{(NH_4)_5[H_2(Mo_2^{VI}O_5)_2(Cr^{III}O_2)\{O_3P\text{-}C(O)(CH_2\text{-}4\text{-}C_5NH_4)PO_3\}_2]\cdot 10H_2O}$ (2a). To a solution of 0.49 g (0.4 mmol) of $(NH_4)_6Mo_7O_{24}\cdot 4H_2O$, 0.18 g (1 mmol) of $Cr_4(SO_4)_5(OH)_2$ and 0.28 g (1 mmol) of 1-hydroxy-2-(4-pyridine) ethylidene-1,1-bisphosphonic acid were added, and the pH was maintained at 6.0, using 25% aqueous ammonia solution. The solution was heated at 60 °C for 1 h with stirring, allowed to cool to room temperature and filtered. The filtrate was kept for slow evaporation and dark green coloured block-shaped crystals of **2a** were obtained after 7 days. Yield: 0.2831 g (4.9% based on chromium). Elemental analysis (%) calculated for **2a**: Mo: 25.35, Cr: 3.57, P: 8.51, C: 11.55, N: 6.73, O: 39.55, H: 3.74. Found: Mo: 26.35, Cr: 3.40, P: 8.28, C: 11.23, N: 6.62, O: 38.90, H: 3.30.

2.1.6 $\mathbf{Na(NH_4)_6[H(Mo_2^{VI}O_5)_2(Mn^{III}O_2)\{O_3P\text{-}C(O)(CH_2\text{-}4\text{-}C_5NH_4)PO_3\}_2]\cdot 9H_2O}$ (3a). To a 20 mL solution of $[Mo_2^VO_4(H_2O)_6]^{2+}$ (2 mmol), 0.1600 g (1 mmol) of $KMnO_4$ was added and the pH was maintained at 1.5 using 25% ammonia solution. Subsequently, to the same solution, 0.5 g (1.80 mmol) of 1-hydroxy-2-(4-pyridyl)-ethylidine-1,1bisphosphonic acid was added and the pH was further increased and maintained at 6.0. The solution was kept for heating at 80 °C for 1 h and then allowed to cool to room temperature and filtered. The filtrate was kept for slow evaporation and yellow coloured block-shaped crystals of **3a** were obtained after a period of 15 days. Yield: 0.059 g (3.9% based on manganese). Elemental analysis (%) calculated for **3a**: Na: 1.57, Mo: 26.23, Mn: 3.75, P: 8.47, C: 11.49, N: 6.70, O: 38.27, H: 3.51. Found: Na: 0.98, Mo: 25.54, Mn: 3.63, P: 8.18, C: 11.39, N: 7.51, O: 38.04, H: 3.28.

2.2 Electrode preparation for cyclic voltammetry

Cyclic voltammogram (CV) studies of pristine compounds **1a–3a** were done at 5 mV s^{-1} in a non-aqueous electrolytic solution of 0.5 M $NaClO_4$ in a ternary solvent mixture of ethylene carbonate, propylene carbonate, and ethyl acetate in a volume ratio of 1 : 1 : 1, using a sample coated directly on glassy carbon as the working electrode, Ag/AgCl (3 M KCl) as the reference electrode and a platinum wire as the counter electrode.

2.3 Preparation of the MWCNT@SS substrate

The preparation of the MWCNT solution followed the reported literature.[63] A thoroughly cleaned stainless steel (SS) substrate was used for MWCNT solution deposition. MWCNT functionalization was carried out to improve surface reactivity during crystal growth on the surface. The process of functionalization was accomplished by refluxing MWCNTs in hydrogen peroxide for 48 hours at 90 °C. After the functionalization, the surface gets added with oxygenated functional groups. Powdered, functionalized MWCNTs were obtained and rinsed with double distilled water (DDW) four to five times before being dried at 60 °C for 12 hours. The MWCNT powder was mixed with Triton X-100 and DDW using an ultrasonication process to acquire a stable and well-dispersed solution. After that, the "dip and dry coating method" was used for depositing MWCNTs on the well-cleaned surface of the SS substrate. These prepared films of the MWCNT-coated SS substrate were subsequently used for the binder-free growth of crystalline phases of **1a**, **2a** and **3a** on the surface of the MWCNT@SS substrate.

2.4 Supercapacitor electrode preparation – direct growth of crystalline phases of 1a, 2a, and 3a on the MWCNT@SS substrate

The growth of compounds **1a**, **2a**, and **3a** on the MWCNT-coated SS substrate was accomplished using a simple dip method. Using a procedure similar to the synthesis of compounds **1a**–**3a**, the prepared MWCNT@SS substrate was vertically dipped in a vial containing the reaction mixture for compounds **1a**–**3a**, respectively, thereby providing nucleation centres for the growth of the crystalline phase of the compounds. After 3–4 days, MWCNT@SS was taken out of the vial and dried at room temperature. The substrate grown electrodes **1-MWCNT@SS**, **2-MWCNT@SS**, and **3-MWCNT@SS** for **1a**, **2a**, and **3a**, respectively, were used as electrodes for electrochemical studies. The weight of the electrodes was recorded before and after deposition, to get the quantity of compounds deposited on MWCNT@SS.

The phase purity of the electrode materials **1-MWCNT@SS**, **2-MWCNT@SS**, and **3-MWCNT@SS** was investigated by powder X-ray diffraction analysis [Fig. S23(a)–(c) in the ESI†]. Prominent and intense peaks were observed in the P-XRD patterns of compounds **1a**, **2a**, and **3a** in electrode materials due to their crystalline nature, and all the major peaks observed for the simulated powder XRD patterns of compounds **1a**, **2a**, and **3a** matched well with the experimental P-XRD patterns of **1-MWCNT@SS**, **2-MWCNT@SS**, and **3-MWCNT@SS**, indicating the phase purity of the crystals grown over MWCNT@SS. The peak present around 25.58° in the pattern of MWCNT@SS corresponds to the lattice plane (002) of graphitic carbon in MWCNTs on the stainless steel. 2θ values of 43.5, 44.3, 50.2, 74.5, and 81.8° correspond to stainless steel. The difference in the intensity of peaks may be due to the change in the orientation of crystals on the film.

Morphological studies of **1-MWCNT@SS**, **2-MWCNT@SS**, and **3-MWCNT@SS** were done by scanning electron microscopy [Fig. 3(a)–(c)]. The electrode material **1-MWCNT@SS** exhibited micro-square block-type crystals on MWCNT@SS, with high grain boundaries of block-type crystals helping in the pseudocapacitive behaviour showing a higher surface contribution with enhanced electrochemical activity due to more electroactive sites for better ion–electrode surface interaction. **2-MWCNT@SS** displayed polygonal-type crystals over the MWCNT-coated stainless steel. Non-uniformity among crystals leads to increased diffusive controlled behaviour for charge contribution due to the inclusion of MWCNTs and their interaction with ions. **3-MWCNT@SS** displayed granular-type crystals with uniform distribution.

EDS analysis was performed for **1-MWCNT@SS**, **2-MWCNT@SS**, and **3-MWCNT@SS**, to tabulate the composition of different atoms present in the compounds of electrode materials [Fig. S25(a)–(c) in the ESI† for **1-MWCNT@SS**, **2-MWCNT@SS**, and **3-MWCNT@SS**, respectively].

3. Results and discussion

3.1 Synthesis and structure

All three complexes were synthesized by the reaction of molybdenum(V) containing $[\mathrm{Mo}_2^{\mathrm{V}}\mathrm{O}_4(\mathrm{H}_2\mathrm{O})_6]^{2+}$ or molybdenum(VI) containing $(\mathrm{NH}_4)_6\mathrm{Mo}_7\mathrm{O}_{24}$, with the respective metal salt, NaVO_3, $\mathrm{Cr}_4(\mathrm{SO}_4)_5(\mathrm{OH})_2$ and KMnO_4, for compounds **1a**, **2a** and **3a**, respectively, and the diphosphonate ligand. As determined from elemental analysis studies, complexes **1a** and **3a** were observed to crystallize as mixed sodium-ammonium salts with the molecular formulae of $\mathrm{Na}_2(\mathrm{NH}_4)_5[(\mathrm{Mo}_2^{\mathrm{VI}}\mathrm{O}_5)_2(\mathrm{V}^{\mathrm{III}}\mathrm{O}_2)\{\mathrm{O}_3\mathrm{PC}(\mathrm{O})(\mathrm{CH}_2\text{-}4\text{-}\mathrm{C}_5\mathrm{NH}_4)\mathrm{PO}_3\}_2]\cdot 10\mathrm{H}_2\mathrm{O}$ and $\mathrm{Na}(\mathrm{NH}_4)_6[\mathrm{H}(\mathrm{Mo}_2^{\mathrm{VI}}\mathrm{O}_5)_2(\mathrm{Mn}^{\mathrm{III}}\mathrm{O}_2)\{\mathrm{O}_3\mathrm{P}\text{-}\mathrm{C}(\mathrm{O})(\mathrm{CH}_2\text{-}4\text{-}\mathrm{C}_5\mathrm{H}_4\mathrm{N})\text{-}\mathrm{PO}_3\}_2]\cdot 9\mathrm{H}_2\mathrm{O}$, respectively, while compound **2a** was observed to crystallize purely as an ammonium salt, $(\mathrm{NH}_4)_5[\mathrm{H}_2(\mathrm{Mo}_2^{\mathrm{VI}}\mathrm{O}_5)_2(\mathrm{Cr}^{\mathrm{III}}\mathrm{O}_2)\{\mathrm{O}_3\mathrm{P}\text{-}\mathrm{C}(\mathrm{O})(\mathrm{CH}_2\text{-}4\text{-}\mathrm{C}_5\mathrm{H}_4\mathrm{N})\text{-}\mathrm{PO}_3\}_2]\cdot 10\mathrm{H}_2\mathrm{O}$. The structures of the compounds were determined using single-crystal X-ray diffraction, which showed that all three complexes have crystallized in the monoclinic crystal system with the centrosymmetric space group $P2_1/n$. Crystallographic information for all three complexes is summarized in Table 1.

The asymmetric unit(s) of the polyanions, $[(\mathrm{Mo}_2^{\mathrm{VI}}\mathrm{O}_5)_2(\mathrm{MO}_2)\{\mathrm{O}_3\mathrm{P}\text{-}\mathrm{C}(\mathrm{O})(\mathrm{CH}_2\text{-}4\text{-}\mathrm{C}_5\mathrm{H}_4\mathrm{N})\text{-}\mathrm{PO}_3\}_2]^{7-}$, where M = V(III), Cr(III), and Mn(III), for polyanions **1**, **2** and **3**, respectively, consists of 24 crystallographically independent atoms, two molybdenum(VI), one 3d-transion metal [vanadium(III), chromium(III) or manganese(III)], two phosphorous, seven carbon, one nitrogen and eleven oxygen atoms, respectively, with the 3d-transion metal(s) residing on a special position with an occupancy of 0.5. The asymmetric unit thus constitutes half of the polyanion and the complete structure is generated *via* symmetry. The polyanion structure resembles an S-shaped assembly of two $\{\mathrm{Mo}_2^{\mathrm{VI}}\mathrm{O}_5\}$-units connected to each other by the central $\{\mathrm{MO}_2\}$ unit [M = V(III), Cr(III) or Mn(III)] and capped by the diphosphonate ligand(s) on either side [see Fig. 1]. The pyridine ring of both diphosphonate ligands within each polyanion are oriented in opposite directions to each other, and the dimeric $\{\mathrm{Mo}_2^{\mathrm{VI}}\mathrm{O}_5\}$- as well as the $\{\mathrm{MO}_2\}$ units are thereby connected to the pentadentate diphosphonate ligand *via* P–O–M, P–O–Mo, and C–O–Mo linkages.

Single-crystal X-ray diffraction (SC-XRD) studies help in the preliminary determination of the oxidation states of the centrally located 3d-transition metal, ostensibly *via* bond-valence-sum calculations, to be +3 [see Tables S1–S3 in the ESI†]. This

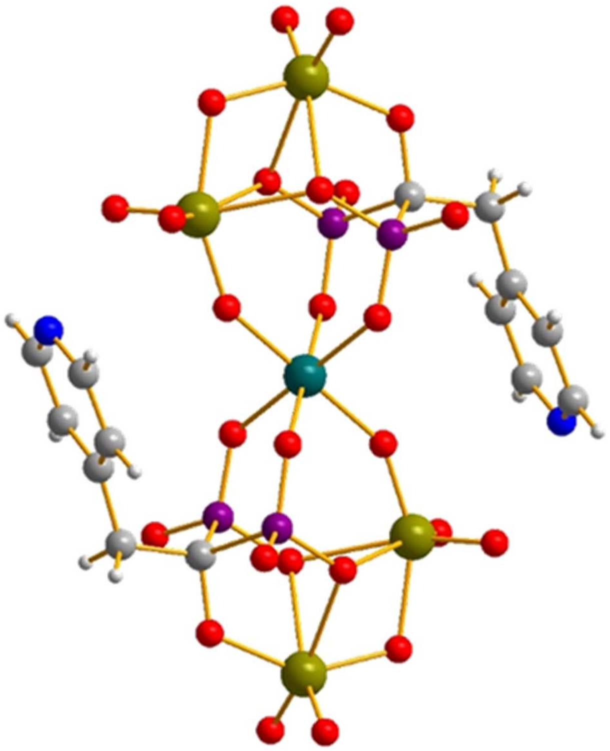

Fig. 1 Ball and stick representation of $[(Mo^{VI}_2O_5)_2(MO_2)\{O_3P\text{-}C(O)(CH_2\text{-}4\text{-}C_5H_4N)\text{-}PO_3\}_2]^{7-}$, where M = V(III), Cr(III), Mn(III), for polyanions **1**, **2** and **3**, respectively. Colour code: yellow, molybdenum(VI); green, vanadium(III)/chromium(III)/manganese(III); purple, phosphorous; red, oxygen; blue, nitrogen; grey, carbon; white, hydrogen.

has been further confirmed by multiple spectroscopic studies (*vide infra*). The synthesis of compounds **1a** and **3a** was done from the reduced molybdenum(V) precursor $[Mo^{V}_2O_4(H_2O)_6]^{2+}$, while the synthesis of **2a** was done from the heptamolybdate anion $[Mo^{VI}_7O_{24}]^{6-}$, where molybdenum is in its highest oxidation state of +6. Thus, during the formation of the compounds **1a** and **3a**, the 3d-transion metal oxometallate anions, the metavanadate $[V^{V}O_3]$ and permanganate $[Mn^{VII}O_4]$, act as oxidizing agents, oxidising Mo(V) to Mo(VI), and themselves getting reduced from +5 to +3 and +7 to +3, for vanadium and manganese, respectively. For compound **2a**, both the chromium and molybdenum sources retain their initial oxidation state(s), from the precursor to the product. Furthermore, with SC-XRD we were also able to determine the arrangement of these ions in the solid state, and it is worth mentioning here that such near identical solid-state assembly of these three different polyanions is directed by the nature of the functional group present on the diphosphonate ligand(s). The symmetric nature of the 4-pyridyl group makes all these structures inherently symmetric, and we have observed that any change in the location of the nitrogen atom position(s) on the aromatic ring plays a direct role in disrupting this symmetry.[64]

With degeneracy present in the d-orbital electronic configuration of vanadium(III) and manganese(III) atoms ([Ar] d^2 and [Ar] d^4 electronic configurations) in polyanions **1** and **3**, respectively, a Jahn–Teller distortion in the metal–oxygen bond(s), needed to break such degeneracy, is observed. Chromium(III), with a d-orbital electronic configuration of d^3, has no such degeneracy present, and therefore none to be lifted *via* a distortion of the metal–oxygen bond(s). Due to the symmetry of the polyanions **1–3**, three sets of metal–oxygen bond distances are observed, 1.952(5), 2.012(5) and 2.019(5) Å, for vanadium–oxygen in polyanion **1**, 1.938(2), 1.985(2), and 1.989(2) Å, for chromium–oxygen in polyanion **2**, and 1.919(3), 2.028(3), and 2.152(2) Å, for manganese–oxygen in polyanion **3** [Tables S1–S3 in the ESI†]. Therefore, the vanadium(III)–oxygen and manganese(III)–oxygen bonds in polyanions **1** and **3**, unlike chromium(III) bonds in polyanion **2**, show severe Jahn–Teller distortion, with a *z*-in type compressed metal–oxygen bond observed, with the compression being slightly larger in Mn–O bond distances compared with V–O bond distances [an average difference of 0.063 *vs.* 0.171 Å between axial and equatorial bond distances in vanadium–oxygen and manganese–oxygen, respectively]. In polyanion **2** however, all three metal–oxygen bonds have similar lengths. As the distortion to lift the degeneracy in the t_{2g} set of orbitals is substantially weaker as compared to the distortion to lift degeneracy in the e_g set of orbitals,[65] the amount of depression in the V–O bond is expectedly less with respect to the manganese–oxygen bond. Distortions in vanadium–oxygen and manganese–oxygen bonds have also been observed in polyanions having similar S-shaped mixed-metal assemblies. While in the polyanions $[(Mo_2O_5)_2(VO_2)\{O_3P\text{-}C(O)(CH_3)\text{-}PO_3\}_2]^{6-}$ and $[(Mo_2O_5)_2(VO_2)\{O_3P\text{-}C(O)(CH_3CH_2CH_2CH_2NH_3)\text{-}PO_3\}_2]^{4-}$, the V–O bonds experience similar *z*-in type distortion [difference in axial *vs.* equatorial bond distances of 0.057 and 0.077 Å, respectively],[66] in the polyanion $[(MnO_2)\{(O_3P\text{-}C(O)(CH_2\text{-}3\text{-}C_5NH_5)\text{-}PO_3)(Mo_2O_5)(MnO_2)(H_2O)(Mo_2O_4)(O_3P\text{-}C(O)(CH_2\text{-}3\text{-}C_5NH_4)\text{-}PO_3)\}_2]_2^{22-}$,[67–70] the Mn–O bonds are observed to undergo a *z*-out type distortion [difference in axial *vs.* equatorial bond distances of 0.248 Å]. And, as expected in the analogous chromium derivative $[(Mo_2O_5)_2(CrO_2)\{O_3P\text{-}C(O)(CH_2\text{-}3\text{-}C_5NH_5)\text{-}PO_3\}_2]^{5-}$, no significant distortion of the Cr–O bond(s) is observed.[67,68] Distortion in the Mn–O bonds has been thoroughly studied with computational methods, to rationalize the stereochemistry of manganese(III) complexes.[71,72]

Phase purity analysis of compounds **1a–3a** was established using powder X-ray diffraction [see Fig. S1–S3 in the ESI†], and the complete composition with the formula was determined using elemental and thermal analysis [see Fig. S4 in the ESI†].

3.1.1 Geometry optimization and energy profile determination.

The geometry optimization of the polyanionic species $[(Mo^{VI}_2O_5)_2(M^{III}O_2)\{O_3PC(O)(CH_2\text{-}4\text{-}C_5NH_4)PO_3\}_2]^{7-}$ [**1′–3′**, M = V (**1′**), Cr (**2′**), Mn (**3′**), see Fig. S5 in the ESI†] and the corresponding reduced anions $[(Mo^{VI}_2O_5)_2(M^{II}O_2)\{O_3PC(O)(CH_2\text{-}4\text{-}C_5NH_4)PO_3\}_2]^{8-}$ [**1′⁻–3′⁻**, see Fig. S6–S8 in the ESI†] was carried out at the B3LYP-D3(BJ)/Def2-SVP level of theory both in the gas phase and in a polar medium (water). The NBO (natural bond orbital) analyses of **1′** show that the LUMO is centred on the central V^{III} ion, which is separated by a bridging oxygen atom attached to a Mo^{VI} ion. The d-orbital of the Mo^{VI} ion also contributes to the LUMO. The LUMOs of Cr (**2′**) and Mn (**3′**) analogues show the involvement of the d-orbitals of both the metal ions (M^{III} and Mo^{VI}), the p-orbital of the bridging oxygen atom and P–O groups. The α-SOMO (singly occupied molecular orbital) and α-SOMO-1 in **1′** represent the d-orbital of the V^{III} atom and the p-orbital of adjacent bridging O atoms. Nearly similar NBO pictures are obtained for Cr (**2′**) and Mn (**3′**) analogues involving α-SOMO-4 (**2′**) and α-SOMO/α-SOMO-2 (**3′**) [see Fig. S9 in the ESI†].

DFT calculations suggest that polyanion **1** possesses a V atom in the +3 oxidation state at the centre, which cannot be unambiguously concluded just from X-ray single crystal bond parameters and BVS calculations alone. The Jahn–Teller contraction (*z*-in) of the V^{III} ion (3d2) in **1** was also noticed in the optimized bond parameters of the polyanion species [Fig. S5(a) in the ESI†]. However, the similar contraction of the Mn^{III} ion (3d4) in complex **3** is mostly favoured by intermolecular interactions, as the DFT calculations of the free polyanion $[(Mo_2^{VI}O_5)_2(Mn^{III}O_2)\{O_3PC(O)(CH_2\text{-}4\text{-}C_5NH_4)PO_3\}_2]^{7-}$ (**3′**) show *z*-out Jahn–Teller elongation [Fig. S5(c) in the ESI†]. For complex **2**, DFT calculations show undistorted Cr^{III} at the centre of the polyanion species [Fig. S5(b) in the ESI†].

3.1.2 Weak interactions and crystal packing. Because of the identical crystal symmetry, the arrangement of the polyanions **1–3** in their respective three compounds **1a–3a** is also observed to be similar along the three dimensions in the solid state. The three-dimensional packing is observed to be directed by intermolecular hydrogen bonding as well as π⋯π stacking interactions. The intermolecular hydrogen bonding arises because of the presence of donor atom(s) from the heteroaromatic ring, the sp^2-hybridized C–H bond, and the acceptor O–Mo group from the $\{Mo_2^{VI}O_5\}$ unit, within the polyanions. The intermolecular hydrogen-bond distances between the donor and the acceptor atoms are in the range of 3.093–3.537 Å, 3.050–3.362 Å, and 3.145–3.432 Å for compounds **1a**, **2a**, and **3a**, respectively [see Tables S7–S9 in the ESI†]. Furthermore, π⋯π stacking interactions can also be considered to be significant in affecting the overall packing arrangement, as the heteroaromatic pyridine rings of the bisphosphonate ligand(s) are observed to be in the range of 3.720–3.684 Å, 3.891–3.947 Å, and 3.891–3.947 Å, for compounds **1a**, **2a** and **3a**, respectively. Along the *a*-axis, each polyanionic unit is thus assembled in a zig-zag manner [see Fig. S10 in the ESI†]. This results in the presence of cavities within such an assembly, occupied by lattice water and counter cations.

3.2 Spectroscopic analysis

Different spectroscopic analyses provided us with invaluable information on the electronic properties and behavior of the atoms within the compounds **1a–3a**. Analysis with different spectroscopic methods, such as infrared, optical, electron paramagnetic resonance and X-ray photoelectron spectroscopy, provided us with a detailed understanding of the behavior of the atoms within each polyanion, which are then correlated with the structure and electrochemical properties.

3.2.1 Infrared spectroscopy. To understand the bonding nature present in the polyanionic assembly, infrared spectroscopy was performed on compounds **1a–3a** in the range of 4000–400 cm^{-1}. As such, the isostructural nature of the polyanions is also evident in the characteristic peaks observed, with all three compounds showing close to identical spectra in the fingerprint region [2000–400 cm^{-1}, see Fig. S11 in the ESI†]. Characteristic peaks corresponding to P–O and P═O stretching vibrations are observed around 1040 and 1140 cm^{-1}.[73] The absorption band appearing around 920–870 cm^{-1} corresponds to various Mo–O bond stretching vibrations[74] and also peaks between 750 and 680 cm^{-1} can be attributed to O–Mo–O bending mode in compounds **1a–3a**.[75] In compound **1a**, peaks observed at 788 and 818 cm^{-1} correspond to V═O and V–O stretching, respectively,[76,77] peaks observed at 535 and 957 cm^{-1} in **2a** are attributed to Cr–O stretching vibrations,[78,79] and peaks at 538 cm^{-1} for **3a** are attributed to Mn–O stretching mode.[80]

3.2.2 X-ray photoelectron spectroscopy. XPS analysis was performed on solid samples of **1a–3a** and on the crystalline phase grown on the MWCNT@SS substrate [see Fig. 2(a–f) for the XPS spectra of **1a–3a**]. The XPS data gave us better insights into the oxidation state of the metal atoms present in the as-synthesized compounds and confirmed the retention of the oxidation states of the compounds upon growth over the MWCNT@SS substrate. All the XPS spectra were corrected with respect to C 1s (284.6 eV) [Fig. S12(a)–S14(a) in the ESI†]. In all three compounds **1a–3a**, the spectral data of molybdenum [Fig. 2(a), (c) and (e) for **1a**, **2a**, and **3a**, respectively] show two deconvoluted peaks at binding energy values of 235.3 and 232.1 eV attributed to $3d_{3/2}$ and $3d_{5/2}$, which confirms the +6 oxidation state of Mo in all three compounds.[81]

The XPS spectra of compound **1a** exhibit V 2p peaks at 522.8 eV and 516.7 eV [Fig. 2(b)], corresponding to V $2p_{1/2}$ and V $2p_{3/2}$, respectively, affirming a +3 oxidation state for the vanadium atom in complex **1**.[82,83] For compound **2a**, the XPS spectra of Cr display two peaks [Fig. 2(d)] at binding energy values of 586.4 eV and 576.6 eV, assigned to Cr $2p_{1/2}$ and Cr $2p_{3/2}$, respectively, confirming the +3 oxidation state of Cr in complex **2**.[84,85] In compound **3a** [Fig. 2(f)], the Mn 2p spectrum displays peaks at 652.5 eV and 640.5 eV, assigned to Mn $2p_{1/2}$ and Mn $2p_{3/2}$, respectively, indicating a +3 oxidation state for manganese in complex **3**.[86] The XPS results thus corroborate the oxidation state values obtained from the BVS calculations for complexes **1–3**, Mo(+6) and M(+3) [M = V, Cr, Mn for complexes **1**, **2**, and **3**, respectively]. The XPS spectra of all remaining elements of compounds **1a**, **2a** and **3a** are given in the ESI [Fig. S12–S14 in the ESI†].

3.2.3 Electron paramagnetic resonance spectroscopy. The XPS bands of the vanadium atom in complex **1** do not unambiguously confirm its formal oxidation state (3+ *vs.* 4+). The spin ground states of V^{IV} and V^{III} are expected to be $S = \frac{1}{2}$ and 1, respectively, which we identified by X-band EPR measurements at 77 K in the solid state.[87–89] The presence of a half-field forbidden signal at $g = 1.989$, corresponding to $\Delta m_s \pm 2$, was observed clearly. Multiple hyperfine lines corresponding to allowed electronic transition at $\Delta m_s \pm 1$ can be attributed to the interaction of coupling of unpaired electrons on the V^{III} centre (^{51}V; 99.8%; $I = 7/2$) with the nuclei of ^{31}P atoms ($I = \frac{1}{2}$) of phosphate groups. The slight unsymmetrical nature of hyperfine lines around the centre of the signal is the manifestation of

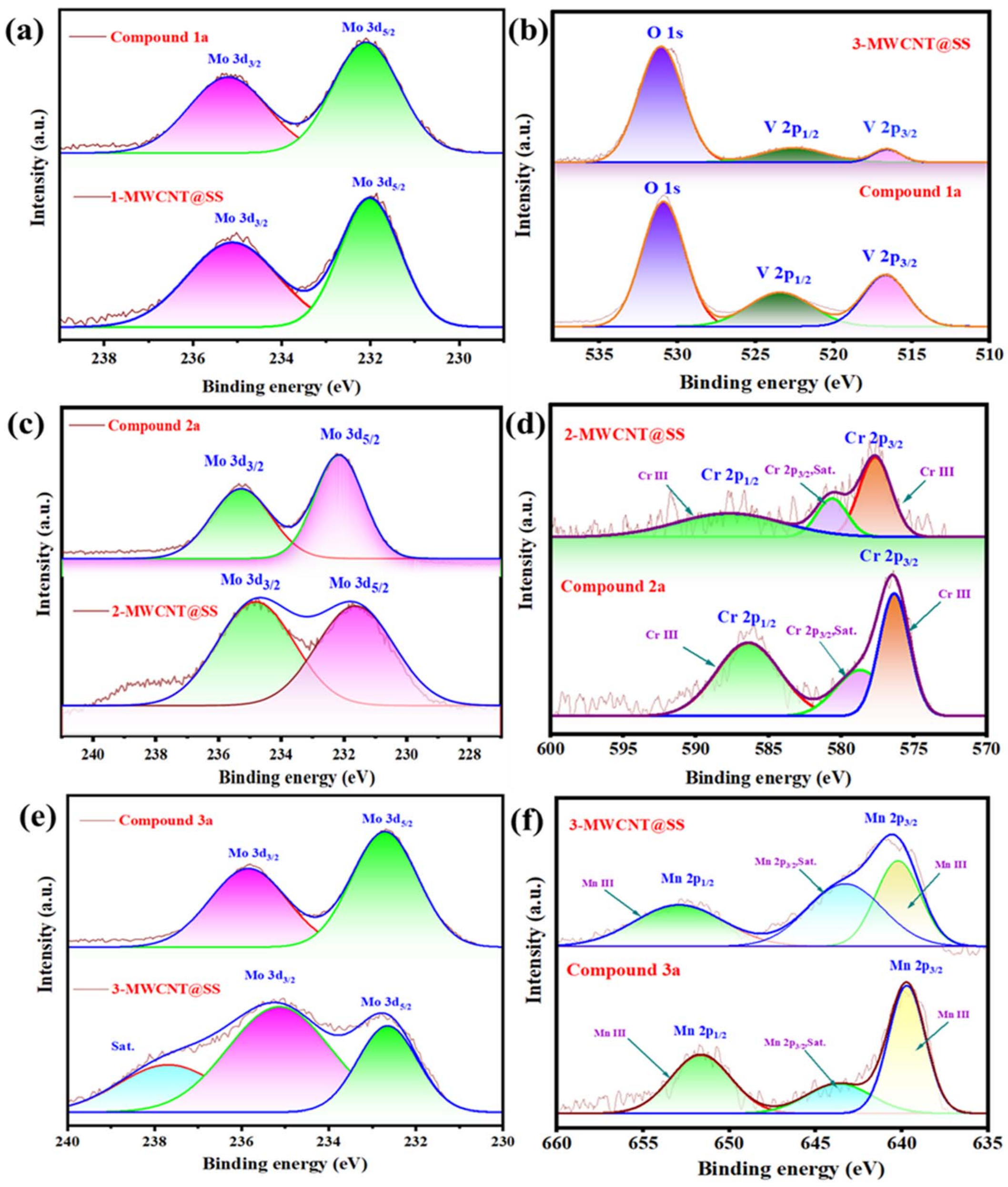

Fig. 2 Comparative XPS spectra of compounds **1a**, **2a** and **3a** with **1-MWCNT@SS**, **2-MWCNT@SS**, and **3-MWCNT@SS**, respectively. (a, c and e) Mo $3d_{3/2}$ and Mo $3d_{5/2}$, (b) V $2p_{1/2}$ and V $2p_{3/2}$ for **1a** with **1-MWCNT@SS**, (d) Cr $2p_{1/2}$ and Cr $2p_{3/2}$ for **2a** with **2-MWCNT@SS**, and (f) Mn $2p_{1/2}$ and Mn $2p_{3/2}$ for **3a** with **3-MWCNT@SS**.

the structural distortion of the coordination geometry of the V^{III} ion in polyanion **1**.

All three complexes display very weak EPR activity at room temperature in aqueous solution at $g = 2$, corresponding to the allowed transition ($\Delta m_s = \pm 1$). However, signals due to both the half-field forbidden transition ($\Delta m_s = \pm 2$) and the allowed transition ($\Delta m_s = \pm 1$) were observed in solid samples at 77 K. The intensities at half-field were stronger for Cr^{III} (**2a**; $g = 1.7621$) [Fig. S16(a) in the ESI†] and Mn^{III} (**3a**; $g = 1.974$) [Fig. S16(b) in the ESI†] complexes than that of V^{III} (**1a**; $g = 1.998$) [Fig. S15 in the ESI†].[90] The unsymmetrical patterns of the EPR signal of these complexes are due to the rhombic nature of these ions. The triplet state of vanadium in complex **1a** was confirmed by the half-field forbidden transition ($\Delta m_s = \pm 2$) in EPR measurements [Fig. S15(a) in the ESI†]. Multiple hyperfine lines were observed for complex **1** in the solid state at 77 K. Complex **2a** possesses a Cr^{III} atom (^{53}Cr; 9.5%; $I = 3/2$), which showed a stronger forbidden signal at $g = 1.7842$ corresponding to $\Delta m_s = \pm 2$, while the corresponding signal for complex **3a**, the Mn^{III} analogue (^{55}Mn, 100%; $I = 5/2$), was noticed at $g = 1.994$. The corresponding signals for $\Delta m_s \pm 1$ are broad in general at 77 K in the solid states of compounds **2a** and **3a**.

The EPR spectrum of complex **1a** in the solid state was simulated with V(III) [$S = 1$, $g_x = 1.9907$, $g_y = 1.99908$, $g_z =$

2.03178, LWPP(1) = 0.2199 mT, LWPP(2) = 0.8177 mT, A_X = 537.269 MHz, A_Y = 322.895 MHz, and A_Z = 190.087 MHz, see Fig. S15 in the ESI†]. From the experimental EPR spectrum of Cr(III) complex **2a** [Fig. S16(a) in the ESI†], the perpendicular *g*-value ($g_\perp$) is 1.688 ($\Delta m = \pm 2$), and the parallel *g*-value ($g_\parallel$) is 2.106 ($\Delta m = \pm 1$).[91] The effective *g*-value derived from the experimental plot is 1.897.[92] To support these experimental findings, a simulation of the same EPR signal was conducted using EasySpin.[93] The simulated *g*-values for g_x, g_y and g_z were determined to be 1.9186, 2.1300, and 2.01047, respectively. The effective *g*-value from the simulated spectrum is 2.01969, which closely approximates the effective *g*-value obtained experimentally, *i.e.*, $g_{\text{eff}} \approx 2$. The g_{iso} value from the simulated spectrum (with the assistance of EasySpin[3]) of Mn(III) complex **3a** [Fig. S16(b) in the ESI†] is 1.8046, which is approximately in accordance with the reference value $g_{\text{iso}} = 1.99(1)$, where $g_{\text{iso}} = [(g_x^2 + g_y^2 + g_z^2)/3]^{\frac{1}{2}}$. Fits were made with *D* limited to positive or negative values, *E* provided an identical sign where appropriate, and *D* limited to $|E/D| \leq 1/3$ since magnetic data are generally immune to *D*'s sign.[90] The *D* and *E* values of the simulated spectrum are 0.59 cm^{-1} and 0.038 cm^{-1} respectively, which are greater than zero according to the reference value $D = +6.9$ cm^{-1} and $E = +0.63$ cm^{-1} respectively.[94] In this study, the $|E/D|$ value is approximately 0.064, which is comparable to the result obtained by Retegan *et al.*, reported as 0.07.[95]

3.2.4 Solution-phase UV-visible spectroscopy. Solution-phase UV-vis studies of compounds **1a**, **2a**, and **3a** were performed in the region from 200 to 800 nm in aqueous solution. Systematic studies of the time-dependent UV-visible spectra were performed to confirm the long-term stability of the synthesized compounds in solution. Charge transfer transitions, observed in the ultraviolet region, dominate the spectra in all three complexes. The strong absorption peak(s) in the range of 210–220 nm are attributed to pπ–dπ ligand metal charge transfer (LMCT) from the terminal oxygen atom (O_t) to molybdenum, while peaks observed in the range of 230–250 nm are attributed to a pπ–dπ charge transition from the bridging oxygen atoms (O_b) of molybdenum [see Fig. S17(a)–(c) in the ESI†].[67] In the visible region, relatively low intensity peaks (corresponding to d–d transitions) were observed in all three complexes. For **1a**, the peak at 430 nm is attributed to $^3T_{1g} \rightarrow {}^3T_{2g}$ [see Fig. S17(a)† inset].[96] For **2a**, two peaks are observed at 456 and 642 nm, attributed to $^4A_{2g} \rightarrow {}^4T_{1g}$ and $^4A_{2g} \rightarrow {}^4T_{2g}$ transitions [see Fig. S17(b)† inset].[97,98] And for **3a**, a broad shoulder, observed at 515 nm, is attributed to the $^5E_g \rightarrow {}^5T_{2g}$ transition [see Fig. S17(c)† inset].[99]

TD-DFT calculations were performed at the B3LYP/def2svp level of theory in order to obtain greater insights into the absorption peaks for each polyanionic species [see Fig. S18–S21 in the ESI†]. For polyanions **1** (V^{III}) and **2** (Cr^{III}), the $\lambda_{\max}$ values obtained from such calculations are within the range of LMCT peaks observed. However, a substantial divergence between the experimental and theoretical $\lambda_{\max}$ values is observed for polyanion **3** (Mn^{III}). Such slight differences in their absorption bands are attributed to the structural differences between modelled structures (**1′**–**3′**) and the polymeric experimental structures (**1a**–**3a**).

3.3 Electrochemical studies – supercapacitor energy storage

Aqueous phase electrochemical studies did not provide us with conclusive oxidation–reduction potential values for the metal atom(s) within each polyanion. This was due to the fact that such values existed beyond −1.23 V [HER potential]. As such to understand the redox properties of the complexes, cyclic voltammetry was performed in an organic solvent mixture, on materials pasted directly on the working electrode [see the Experimental section]. Cyclic voltammograms collected using this method provided us with distinct oxidation–reduction peak potentials for all three compounds [see Fig. S22 in the ESI†]. Compound **1a** displays a single oxidation peak at −0.67 V and a reduction peak at −1.04 V *vs.* Ag/AgCl. For compound **2a**, two distinct oxidation peaks are observed at −0.67 and −0.27 V as well as two distinct reduction peaks at −0.69 and −0.897 V *vs.* Ag/AgCl. For compound **3a**, single oxidation reduction peaks are observed as well, with the oxidation peak potential observed at 0.225 V and the reduction peak potential observed at −0.69 V *vs.* Ag/AgCl.

Having observed the good redox behaviour of the three compounds **1a**–**3a** in solution, we subsequently endeavoured to explore their applications with respect to energy storage capabilities as supercapacitor(s). Electrochemical studies were now undertaken with the compounds in a heterogeneous phase with respect to electrolyte, with electrodes fabricated by the growth of crystalline phases of the compounds on supporting substrates. In order to get a reliable comparative understanding of the activities of the three polyanions, our earlier used binder-free approach was employed to grow films of crystalline compounds on multi-walled carbon nanotubes on a stainless steel substrate (MWCNT@SS). The choice of this particular substrate has multiple advantages, including the formation of durable electrodes for multiple redox cycles and hybrid supercapacitive behaviour from these compounds, resulting in better performance. Thus, besides providing a robust support for the growth of films of the redox active material(s), possible owing to the strong interactions of the polyanions with the CNT material, the MWCNT@SS substrate also provided electrochemical double layer capacitance properties, which in conjunction with the pseudocapacitive behaviour of the polyanions resulted in the highly desired hybrid supercapacitor activity. The electrodes thus obtained are labelled as **1-MWCNT@SS**, **2-MWCNT@SS**, and **3-MWCNT@SS** for compounds **1a**, **2a**, and **3a**, respectively [see the Experimental methods for the detailed procedure]. To confirm the validity and purity of phases grown on the MWCNT@SS substrate, the electrodes were thoroughly characterized using powder X-ray diffraction [Fig. S23 in the ESI†], as well as X-ray photoelectron spectroscopy [Fig. 2] and infrared spectroscopic methods [Fig. S24 in the ESI†]. The morphology of the phases grown on the MWCNT@SS substrate was characterized with scanning electron microscopy imaging [see Fig. 3(a)–(c) for **1-MWCNT@SS**–**3-MWCNT@SS**, respectively], confirming the crystalline nature of such phases, and their elemental composition was established with EDX spectra and tabulated [Fig. S25(a)–(c) and Table S10 in the ESI†].

Preliminary electrochemical investigations of the electrodes **1-MWCNT@SS**, **2-MWCNT@SS** and **3-MWCNT@SS** were

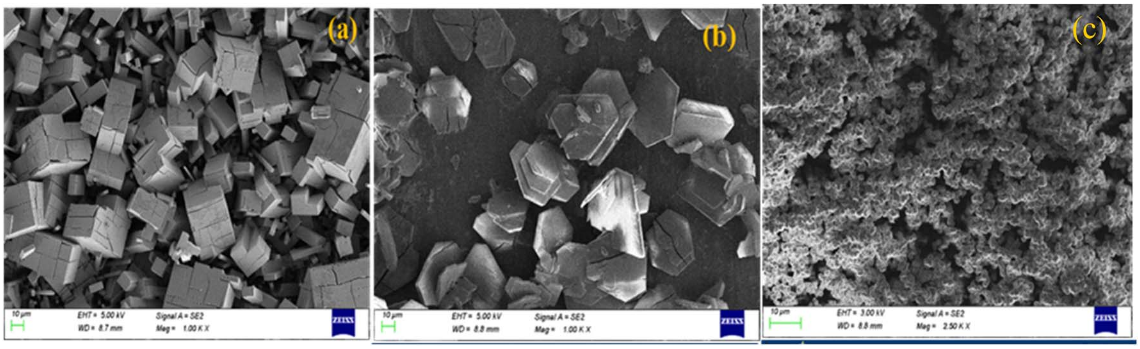

Fig. 3 (a–c) FESEM images of **1-MWCNT@SS**, **2-MWCNT@SS** and **3-MWCNT@SS**, respectively.

performed by cyclic voltammetry (CV) studies with a three-electrode system having **1-MWCNT@SS**, **2-MWCNT@SS** or **3-MWCNT@SS** as the working electrode, Ag/AgCl (3 M KCl) as the reference electrode and a platinum rod as the counter electrode, in 0.5 M $NaClO_4$ electrolyte solution in a ternary mixture of organic solvents ethyl acetate, ethylene carbonate, and propylene carbonate. Additionally, galvanostatic charge–discharge (GCD), and electrochemical impedance spectroscopy (EIS) provided us with data on their energy storage capabilities. The specific capacitances (C_s), energy density (E) and power density (P) of all the **1-MWCNT@SS**, **2-MWCNT@SS**, and **3-MWCNT@SS** electrode materials were calculated using the following equations from the CV and GCD data.[100]

Specific capacitance (C_s):

$$C_s = \frac{1}{m \times v \times \Delta V}\int I(V)\mathrm{d}V \tag{1}$$

where m, v, and ΔV represent the active material mass, scan rate, and potential window.

Specific capacitance (C_s):

$$C_s = \frac{2I\int V\mathrm{d}t}{m\left(v_f - v_i\right)^2} \tag{2}$$

where I, m, $(v_f - v_i)$, and $\int V\mathrm{d}t$ represent the current, mass, potential window, and area under the experimental discharge curve, respectively.

The energy density, E, and power density, P, are expressed by the following equations:[101]

$$E = \frac{1}{2}\frac{C_s(\Delta V)^2}{3.6} \tag{3}$$

$$P = \frac{E}{\Delta t(\mathrm{s})} \times 3600\ \mathrm{W\ kg^{-1}} \tag{4}$$

where E, P, Δt, C_s, and ΔV represent the energy density, power density, discharge time in seconds, capacitance, and potential window.

3.3.1 Cyclic voltammetry. The electrochemical properties of electrodes prepared with **MWCNT**, **1-MWCNT@SS**, **2-MWCNT@SS**, and **3-MWCNT@SS**, respectively, were examined through cyclic voltametric (CV) studies with varying scan rates in the range of 5–100 mV s^{-1}, starting from higher to lower values of scan rates. The vanadium-based electrode **1-MWCNT@SS** was observed to exhibit the highest potential window, showing a potential range from −1.5 to +0.5 V, followed by the chromium-based **2-MWCNT@SS** electrode showing a potential range of −1.155 to +0.5 V, and subsequently the manganese-based **3-MWCNT@SS** electrode showing the lowest potential range of −0.93 to +0.5 V [Fig. 4(a)–(c)]. For all three electrodes, the starting potential range was observed to occur at a negative value with respect to the maximum positive potential of +0.5 V. As such, with values of +2, +1.655, and +1.43 V, for vanadium, chromium and manganese-based electrode(s), respectively, the highest potential window was observed for the vanadium-based electrode **1-MWCNT@SS**. Such a behaviour well matched with our theoretical analysis of the electronic properties of the polyanions themselves.

The quasi-rectangular shape of the CV curve [Fig. 4(a)–(c)] indicates the pseudocapacitive nature of the hybrid electrode(s), combining the behaviour of the pseudocapacitive of the oxometallate polyanion and the EDLC supercapacitance of MWCNTs.[102] With increased values of the scan rate, a shift in the CV curve occurs towards high current density values, ostensibly due to the increased polarization over the electrode surface. The scan rate affects the transport of electrons as well as electrolytic ion diffusion on the surface of the electrode. Lower scan rates tend to support effective ionic transport, leading to high specific capacitance values, while the reverse phenomenon occurs at high scan rates, due to insufficient time for the interaction of ions with the external and internal active sites on the electrode material. With specific capacitance values of 640 F g^{-1}, 256 F g^{-1}, and 132 F g^{-1} for electrodes **1-MWCNT@SS**, **2-MWCNT@SS** and **3-MWCNT@SS**, respectively, at a particular scan rate of 5 mV s^{-1}, the vanadium electrode also shows the best redox efficiency [see Fig. 4(d) and (e) for the comparative CV curves and specific capacitances of **1-MWCNT@SS**, **2-MWCNT@SS** and **3-MWCNT@SS**, respectively]. The area under the CV curve along with the potential window thus follows the order of **1-MWCNT@SS** > **2-MWCNT@SS** > **3-MWCNT@SS**. From the above results, we can clearly infer that the vanadium-based **1-MWCNT@SS**, with its higher specific capacitance values, exhibits the best performance, in comparison with the chromium-based **2-MWCNT@SS** and manganese-based **3-MWCNT@SS**. Such a behaviour can once again be explained on the basis of the high redox efficiency of V^{3+} in **1-MWCNT@SS**.

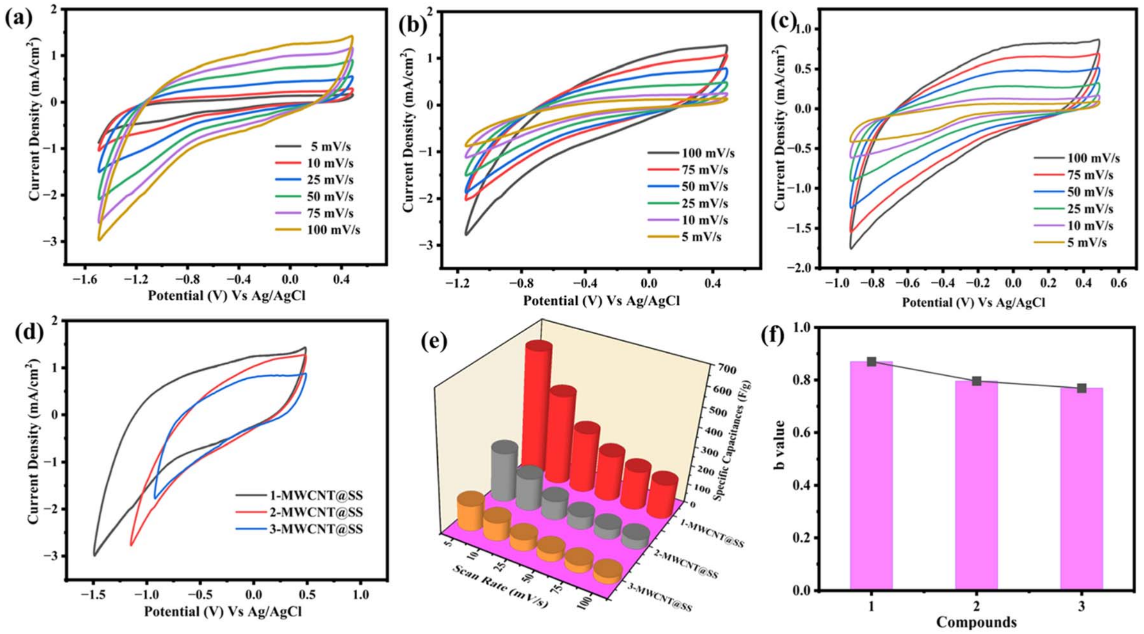

Fig. 4 Electrochemical performance of the prepared electrodes in 0.5 M $NaClO_4$ electrolyte solution. (a–c) CV plots of **1-MWCNT@SS**, **2-MWCNT@SS** and **3-MWCNT@SS** with varying scan rates of 5–100 mV s^{-1}. (d) Comparative CV plots of **1-MWCNT@SS**, **2-MWCNT@SS** and **3-MWCNT@SS** at a scan rate of 100 mV s^{-1}. (e) Comparative specific capacitance plots of **1-MWCNT@SS**, **2-MWCNT@SS** and **3-MWCNT@SS**. (f) Comparative *b*-values of **1-MWCNT@SS**, **2-MWCNT@SS** and **3-MWCNT@SS**.

Compounds **1a**, **2a** and **3a** contain isostructural and identically charged anionic species, balanced by sodium and/or ammonium ions. During the electrochemical process, electrolyte ion diffusion occurs on the electrode surface, with charge storage primarily facilitated by the intercalation and deintercalation of the Na^+ ions from the electrolytic solution and therefore present in excess, accompanied by faradaic redox reactions.[103] The plausible reaction mechanism for polyanions **1–3** is hence summarized as follows:

$$[(Mo_2^{VI}O_5)_2(M^{III}O_2)\{O_3P\text{-}C(O)(CH_2\text{-}4\text{-}C_5H_4N)\text{-}PO_3\}_2]^{7-} + zNa^+ + ze^- \leftrightarrow [(Mo_2^{VI}O_5)_2(M^{III\text{-}z}O_2)\{O_3P\text{-}C(O)(CH_2\text{-}4\text{-}C_5H_4N)\text{-}PO_3\}_2]Na_z^{(7+z)-}$$

The above equation involves one of the electrochemical redox reactions associated with the $M^{II}–e^- \leftrightarrow M^{III}$ pair [M = V, Cr, Mn].[104,105]

The internal charge contribution is explained using the power law, on the basis of the scan rate ($i_P = av^b$), with the *b* value generally lying in the range of 0 to 1 [a *b* value of 1 refers to surface-contributed mechanisms, whereas a value of 0.5 refers to diffused controlled mechanisms].[106] The *b* value can thus be determined from a plot of $\log(i_p)$ *vs.* $\log(v)$ at different voltages in the potential window of **1-MWCNT@SS**, **2-MWCNT@SS** and **3-MWCNT@SS** [Fig. S26(d)–(f) in the ESI†]. Comparative b-values [shown in Fig. 4(f)] depict that **1-MWCNT@SS** (with an average *b* value of 0.87) has a mixed contribution of both surfaces as well as the diffusive charge phenomenon in the charge storing mechanism. **2-MWCNT@SS** and **3-MWCNT@SS** show *b* values of 0.79 and 0.76, respectively, also indicating a mixed combination of capacitive and diffusion-controlled processes similar to **1-MWCNT@SS.** Such a phenomenon can be attributed to the hybrid electrode material behaviour. The higher *b*-value for **1-MWCNT@SS** corresponds to a mechanism where surface contributions are more significant. The overall charge generated at the electrode surface is the summation of the surface charge at the electrolyte and at the electrode interface, where diffusive charges arise from the redox reaction over the electrode surface, given by the semi-infinite linear graph [as shown in Fig. S26(a)–(c) in the ESI†]. The ratio of the overall charge contribution from the electrode materials **1-MWCNT@SS**, **2-MWCNT@SS**, and **3-MWCNT@SS** is given in Fig. 5(a)–(c). As such, surface capacitive charge increases and diffusive controlled charge decreases with increasing scan rate from 5–100 mV s^{-1}**.** **1-MWCNT@SS** shows a more diffusive contribution of 72% and a surface capacitive contribution of 28% at a scan rate of 100 mV s^{-1}, indicating the dominance of diffusive contribution as well as a high surface capacitive contribution, due to the wide potential range [−1.5 to +0.5 V]. In a similar way, electrodes **2-MWCNT@SS** and **3-MWCNT@SS** exhibit enhanced diffusive controlled charge contribution over the surface charge with respect to decreased scan rates. This can be attributed to the low potential window and morphology variation on the surface of the electrodes. Thus, the charge contribution of the electrodes involves both diffusive controlled and surface charge capacitive processes. However, the contribution of the diffusive controlled process mainly dominates over the surface charge capacitive for the overall internal charge of the electrodes due to the covering of grown crystals of compounds on the electrode surface.

3.3.2 Galvanostatic charge–discharge (GCD) measurements. In order to assess the electrochemical activity with their

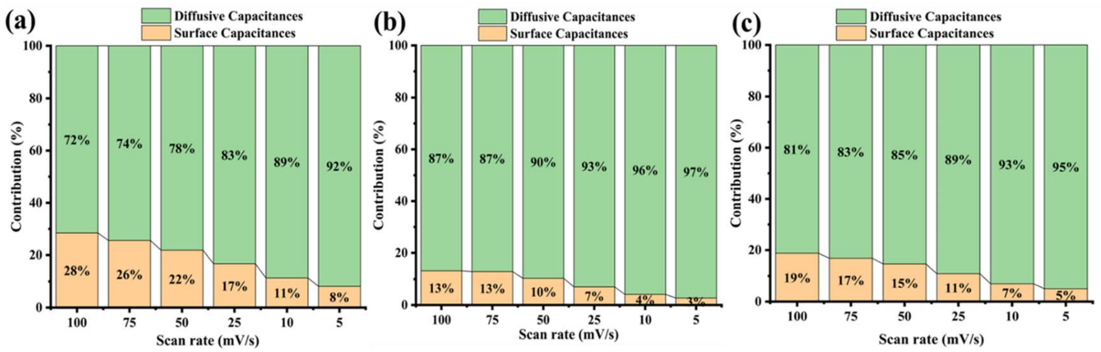

Fig. 5 Charge contribution profiles for (a) **1-MWCNT@SS**, (b) **2-MWCNT@SS**, and (c) **3-MWCNT@SS**, at varying scan rates from 5–100 mV s^{-1}.

respective potential ranges, as well as their energy storage efficiencies, GCD studies of the as prepared electrodes **1-MWCNT@SS**, **2-MWCNT@SS**, and **3-MWCNT@SS** were conducted with variable current density values [chosen as per the response of the electrode] in the same electrolytic medium. Fig. 6(a) shows the GCD plots for the vanadium-based **1-MWCNT@SS**, at current densities of 0.4, 0.8, 1.2, 1.6, and 2 mA cm^{-2}, giving specific capacitance values of 42.82, 30.55, 21.19, 23.82, and 9.26 F g^{-1}, respectively. From the GCD plot for chromium-based **2-MWCNT@SS** [Fig. 6(b)], at current density values of 1.0, 1.2, 1.4, 1.6, and 1.8 mA cm^{-2}, specific capacitances were obtained as 48.83, 35.78, 29.71, 23.78, and 19.89 F g^{-1}, respectively. And, from the GCD plot for manganese-based **3-MWCNT@SS** [Fig. 6(c)], at current densities of 0.4, 0.8, 1.2, 1.6, and 2 mA cm^{-2}, specific capacitances were obtained as 14.64, 8.82, 7.45, 6.88, and 6.83 F g^{-1}, respectively. From the comparative plot of GCD measurements for **1-MWCNT@SS**, **2-MWCNT@SS**, and **3-MWCNT@SS**, at a common current density value of 1.6 mA cm^{-2}, it is clearly observed that the vanadium-based electrode **1-MWCNT@SS** shows the highest discharge time of 20.5 s, followed by the chromium-based **2-MWCNT@SS**, with a discharge time of 15.66 s, and finally the manganese-based **3-MWCNT@SS**, with a discharge time of 4.79 s [Fig. 6(d)]. Furthermore, with a discharging specific capacitance of 23.82, 23.78 and 6.88 F g^{-1} for vanadium, chromium and manganese, respectively, the electrochemical activity trend of the electrodes as well as the electrode materials can be inferred as **1-MWCNT@SS** (vanadium) > **2-MWCNT@SS** (chromium) > **3-MWCNT@SS** (manganese). This trend is consistent with the results obtained from the CV studies, wherein **1-MWCNT@SS** showed the highest activity, whereas **3-MWCNT@SS** had the lowest activity.

Ragone plots show the correlation between the energy density and power density of an electrode material. Fig. 6(e) depicts the comparative Ragone plots for **1-MWCNT@SS**, **2-**

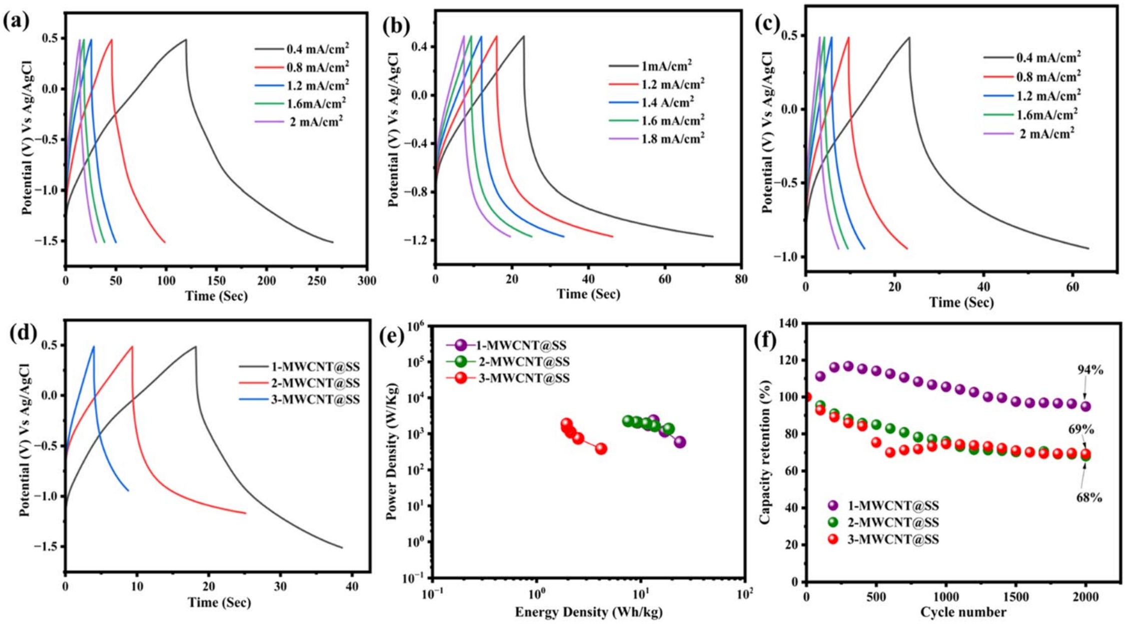

Fig. 6 Electrochemical performance of the prepared electrodes in 0.5 M $NaClO_4$ electrolyte solution, GCD plots of (a) **1-MWCNT@SS**, (b) **2-MWCNT@SS** and (c) **3-MWCNT@SS**, with varying current densities (mA cm^{-2}), (d) comparative GCD plots of **1-MWCNT@SS**, **2-MWCNT@SS** and **3-MWCNT@SS** at a current density of 1.6 mA cm^{-2}, (e) comparative Ragone plots of **1-MWCNT@SS**, **2-MWCNT@SS** and **3-MWCNT@SS**, and (f) comparative electrochemical stability plots of **1-MWCNT@SS**, **2-MWCNT@SS** and **3-MWCNT@SS**.

MWCNT@SS, and **3-MWCNT@SS**. As expected, **1-MWCNT@SS** shows the highest energy density of 13.23 W h kg^{-1} with the highest power density of 2324 W kg^{-1}. This is followed by **2-MWCNT@SS**, with an energy density of 9.04 W h kg^{-1} at a power density of 2079.9 W kg^{-1}. And finally, **3-MWCNT@SS** gives an energy density of 1.95 W h kg^{-1} at a power density value of 1469.72 W kg^{-1}.

3.3.3 Electrochemical impedance spectroscopy (EIS) studies. In order to analyse the interfacial properties at the electrode surface during the electrochemical process of our as-prepared electrodes, electrochemical impedance spectroscopy (EIS) studies were performed at varying frequency values. The purpose behind such EIS studies is to obtain information about the reaction kinetics and mechanisms in these electrochemical systems. As such, EIS is crucial in the study of energy storage and conversion devices. It provides insights into the electrochemical performance, charge transfer processes, and other parameters that affect the efficiency of these devices, and in our case, it is extremely useful to gauge the relative efficiency of the three compounds and their respective electrodes.

To interpret the relationship between the specific capacitance of electrode materials and resistances faced, EIS studies of the electrodes **1-MWCNT@SS**, **2-MWCNT@SS**, and **3-MWCNT@SS** were performed in the frequency range of 100 000 Hz to 0.1 Hz. The Nyquist plots of **1-MWCNT@SS**, **2-MWCNT@SS**, and **3-MWCNT@SS**, a plot of the real part of the impedance (Z') on the x-axis *vs.* the imaginary part of the impedance (Z'') on the y-axis, are shown in Fig. 7(a)–(c), respectively [the fitting circuit is shown as an inset in the plot]. The Nyquist plot is particularly useful for analysing processes like charge transfer reactions, diffusion, and adsorption in electrochemical systems, and the size and shape of features in the plot can provide insights into the kinetics of these processes, the resistance of the electrolyte, the double-layer capacitance, and other important parameters. For our purposes, charge transfer resistance (R_{ct}) and solution resistance (R_s) are the main parameters obtained from the Nyquist plot. R_{ct} and R_s influence the specific capacitance values with increased resistance. The high-frequency region in the Nyquist plot provides R_s with an intersection on the x-axis. R_{ct} arises from the semicircular curve in the region of high frequency.

Table 2 The R_s, R_{ct}, and R_L values of 1-MWCNT@SS, 2-MWCNT@SS and 3-MWCNT@SS electrodes

Electrode materials	R_s (Ω)	R_{ct} (Ω)	R_L (Ω)
1-MWCNT@SS	6.56	107.7	9.66
2-MWCNT@SS	62.84	264	8900
3-MWCNT@SS	26.83	223.2	3500

A comparative summary of the R_s and R_{ct} values for the electrodes **1-MWCNT@SS**, **2-MWCNT@SS**, and **3-MWCNTs@SS** is presented in Table 2. The vanadium-based **1-MWCNT@SS** shows a low R_{ct} value of 107.7 Ω, indicating better charge transfer across the electrode–electrolyte interface, resulting in its high specific capacitance. This also indicates the greater ease of oxidation and/or reduction of the V^{3+} centre, facilitating the redox reactions, and can be associated with the faster electron transfer kinetics across the electrode interface. **2-MWCNT@SS** and **3-MWCNT@SS** containing Cr^{3+} and Mn^{3+} gave measured R_{ct} values of 264 and 223.2 Ω, respectively, which indicate lower charge transfer kinetics at the interface of the electrode. Furthermore, **1-MWCNT@SS**, **2-MWCNT@SS**, and **3-MWCNT@SS** show measured R_s values of 6.56, 62.84, and 26.83 Ω, respectively. The relatively low R_s of **1-MWCNT@SS** can also be attributed to the better multielectron transfer tendency of the V^{3+} system, which is able to reduce the intrinsic resistance of the electrolyte–electrode interface with the acceleration of charge transfer. **2-MWCNT@SS** shows high R_s due to the feeble electron transfer from the stable configuration of the half-filled d^3 electronic system of Cr^{3+}. However, the higher specific capacitance of **2-MWCNT@SS** compared to **3-MWCNT@SS** indicates that the ease of the redox process determines the overall solution resistance provided by the electrode. Diffusive contributions [as shown in Fig. 5(a), a comparative graph of the diffusive and surface contributions] also have important effects on such systems, and a multi-factor combination leads to the overall charge transfer as well as surface resistance of the electrodes to the circuit.[106] Therefore, from the EIS results, it can be again observed that the vanadium-based **1-MWCNT@SS** shows a relatively higher ion conductivity, good electroactivity, and enhanced capacitive performance as compared to the chromium-based **2-**

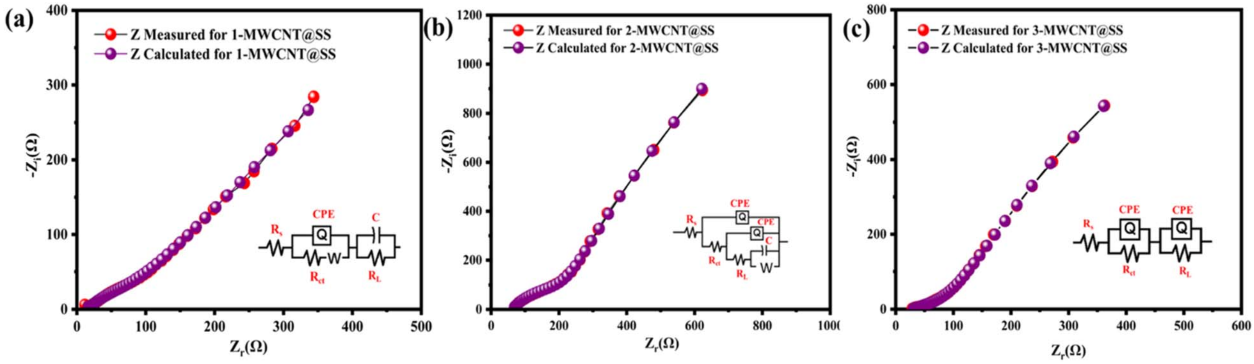

Fig. 7 Electrochemical impedance spectroscopy (EIS) analysis: Nyquist plots of (a) 1-MWCNT@SS, (b) 2-MWCNT@SS, and (c) 3-MWCNT@SS. Fitting circuit is shown as an inset.

Table 3 Comparative data for electrochemical studies (potential window, specific capacitance, power density, energy density and capacity retention rates)

Electrode materials	Potential window (V)	Specific capacitance (F g^{-1})	Power density (W h kg^{-1})	Energy density (W kg^{-1})	Capacity retention (%)
1-MWCNT@SS	−1.5 to +0.5	640	2324.0	13.23	98
2-MWCNT@SS	−1.155 to +0.5	256	2079.9	9.04	68
3-MWCNT@SS	−0.93 to +0.5	132	1469.7	1.95	69

MWCNT@SS and manganese-based **3-MWCNT@SS.** With smaller values of R_{ct} and R_s, which are attributed to the richness of redox activity in hybrid inorganic organic polyoxomolybdate complexes, V^{3+} shows the greatest efficiency.

3.3.4 Stability tests. The electrochemical cycling stability of the electrodes **1-MWCNT@SS**, **2-MWCNT@SS**, and **3-MWCNT@SS** was determined for 2000 CV cycles at a scan rate of 300 mV s^{-1}, within their optimized potential ranges. Fig. 6(f) shows the comparative cycling stability plots of all three electrodes, which exhibit initial specific capacitance retentions of 98%, 68%, and 69% for the electrodes **1-MWCNT@SS**, **2-MWCNT@SS**, and **3-MWCNT@SS**, respectively [for graphs of 2000 CV cycles with an interval of 100 CV cycles see Fig. S27 in the ESI†]. This indicates the superior charge retention efficiency and the superior reversible electron transfer tendency, without altering the structural topology and properties of the vanadium-based electrode **1-MWCNT@SS**. The **2-MWCNT@SS** electrode displays a linear decrease in the stability curve with respect to the number of cycles, with a capacity retention of 68% at the end of 2000 CV cycles. For the electrode **3-MWCNT@SS**, an initially stable nature of the linear curve until 100 cycles is followed by a steep decrease in the specific capacitance, with a final specific capacitance retention of 69% reached after 2000 CV cycles. These can be attributed to the changing faradaic redox process, ostensibly due to the dislodging of a very small number of granular crystals from the electrode surface. Thus **1-MWCNT@SS** is notably observed to be more stable over extended redox cycles, as compared with the **2-MWCNT@SS** and **3-MWCNT@SS** electrodes, both of which show nearly equal stability after capacity retention. To investigate the integrity of electrode materials after cycling stability tests, we have carried out P-XRD measurements of the electrode materials before and after the electrochemical analysis [Fig. S28 in the ESI†]. The prevalence and shape of the P-XRD pattern, before and after analysis, confirm the stable nature of the compounds during the electrochemical process.

3.4 A comparative analysis of the electrochemical behavior – correlation with theoretical studies

From the electrochemical studies of the bare compounds **1a–3a**, pasted on the working electrode, the better redox activity of the vanadium-containing complex is clearly observed. Compound **1a** having V(III) atoms shows a higher reduction potential of −1.03 V, as compared to compound **2a** with Cr(III) showing a redox potential of −0.89 V and compound **3a** containing Mn(III) atoms showing a redox potential of −0.65 V.

The greater efficiency of **1a** with respect to **2a** and **3a** is further corroborated by the extensive studies of its supercapacitor properties. Our binder-free approach to preparing such electrodes makes it possible to compare the solid-state electrochemical and energy storage performance between these three systems. All such studies show the highest performance for the vanadium(III) system [Table 3]. In cyclic voltametric studies, the vanadium(III)-based electrode exhibits the widest potential window. Specific capacitance values also show the superior performance of the vanadium compound, with the obtained values of 640, 256, and 132 F g^{-1}, for vanadium(III) containing **1-MWCNT@SS**, chromium(III) containing **2-MWCNT@SS**, and manganese(III) containing **3-MWCNT@SS**, respectively. Subsequently, from GCD studies vanadium(III) and chromium(III) show the highest potential, with discharging specific capacitance values of 23.82, 23.78 and 6.88 F g^{-1} for **1-MWCNT@SS**, **2-MWCNT@SS** and **3-MWCNT@SS**, respectively. Finally, with energy density values of 13.23, 9.04, and 1.95 W h kg^{-1} and power density values of 2324, 2079.9, and 1469.72 W kg^{-1} for **1-MWCNT@SS**, **2-MWCNT@SS** and **3-MWCNT@SS** systems, respectively, the vanadium(III)-based **1-MWCNT@SS** showed the best performance. The vanadium(III)-based system also outperformed the other two electrodes in the cycling stability test for 2000 CV cycles with an initial specific capacitance retention of 98%. Solution and charge transfer resistances, obtained from the EIS studies, also showed substantially lower values for the vanadium(III)-based electrode. Therefore, from the above comparative correlation, it can be concluded that the vanadium(III)-based **1-MWCNT@SS** shows significantly better efficiency when compared with the chromium(III) and manganese(III) systems.

This trend in electrochemical behaviour has been established with our theoretical studies on the relative ease of oxidation–reduction for all three compounds. To rationalize the redox behaviour and the relative electrochemical performances, the oxidation–reduction propensity of the corresponding complexes **1–3** was studied using DFT calculations. DFT calculations suggest that central paramagnetic atoms [V(III), Cr(III) or Mn(III)] play a significant role in the supercapacitor activity of complexes **1a–3a**, assisting the electronic transport *via* the participation of the d-orbitals of the central metal atoms and their oxidation/reduction ($V^{II/III}$, $Cr^{II/III}$, and $Mn^{II/III}$). DFT calculations further suggest that the polyanions with 7- charge [Fig. S5†] are comparatively more stable than corresponding 8-anions in the gas phase, while the trend is shown to be reversed in polar solvent [Fig. S7–S9 in the ESI†]. The reduction of V^{3+} (**1′**) to V^{2+} (**1′**$^-$), Cr^{3+} (**2′**) to Cr^{2+} (**2′**$^-$), and Mn^{3+} (**3′**) to Mn^{2+} (**3′**$^-$) is favorable by ∼−47, −58, and −81 kcal mol^{-1}, respectively, in water medium. Conversely the trend of the oxidation of the reduced species is observed to be $\mathbf{1'^{-}} \rightarrow \mathbf{1'}$ ($V^{2+} \rightarrow V^{3+}$) > $\mathbf{2'^{-}} \rightarrow \mathbf{2'}$ ($Cr^{2+} \rightarrow Cr^{3+}$) > $\mathbf{3'^{-}} \rightarrow \mathbf{3'}$ ($Mn^{2+} \rightarrow Mn^{3+}$). Also, the trend of the computed HOMO–LUMO energy gaps of $\mathbf{1'^{-}}$–$\mathbf{3'^{-}}$ is V═Cr < Mn. Further calculations showed that protonation at the N atom in **1′**–**3′** can further facilitate the electron transfer process by ~3–4 kcal mol^{-1} only. The HOMO–LUMO energy gaps and the corresponding NBOs are given in the ESI† [Table S5 in the ESI†].

4. Conclusions

In conclusion, three newly synthesized 3d–4d metal-based hybrid polyoxomolybdates, having an S-shaped structure containing two {Mo_2O_5} units connected *via* a central 3d metal [vanadium (**1a**), chromium (**2a**) and manganese (**3a**)], and capped with a diphosphonate ligand, have been synthesized and structurally characterized. All three complexes are observed to be isostructural and crystallize in the identical space group of $P2_1/n$. Bond-valence-sum calculations, as well as XPS and EPR spectroscopic studies, show that the 3d-transition metals V, Cr, and Mn are all in a +3 oxidation state. In order to study the effect of electrons in the d-orbitals of central 3d metals on their electrochemical properties, electrodes were prepared by growing crystalline-phase films on multi-walled carbon nanotubes on a stainless steel substrate (**MWCNT@SS**). The electrodes thus prepared **1-MWCNT@SS**, **2-MWCNT@SS**, and **3-MWCNT@SS** for complexes **1a**, **2a**, and **3a**, respectively, were subjected to electrochemical supercapacitor performance analysis in an electrolytic solution of 0.5 M $NaClO_4$ in a ternary solvent mixture of ethylene carbonate, propylene carbonate, and ethyl acetate in a volume ratio of 1 : 1 : 1. The electrode **1-MWCNT@SS** was observed to show superior performance, with respect to the other two, in terms of potential window, specific capacitance, energy density, power density, solution and charge transfer resistance, and cycling stability retention rates. The comparative correlation of all the above properties showed that the V^{III} based (d^2 electron) system of **1-MWCNT@SS** shows better electrochemical performance as compared to Cr^{III} based (d^3) and Mn^{III} based (d^4 electron) systems, with an electrochemical performance trend of **1-MWCNT@SS** > **2-MWCNT@SS** > **3-MWCNT@SS**. This has also been corroborated by theoretical studies on the ease of oxidation–reduction for all three complexes, which confirms the above trend. DFT calculations suggest that these complexes can most likely be classified as pseudo-supercapacitors. The electrochemical redox reaction is associated with the $M^{II}–e^{-} \leftrightarrow Mn^{III}$ pair [$M = V, Cr, Mn$]. The complexes containing the former divalent metal ion (vanadium) are more stable in polar solvent.

Data availability

CCDC 2345425–2345427 contain the supplementary crystallographic data for this paper.†

Author contributions

Kalyankumar S. Morla: methodology, formal analysis, investigation, data curation, and writing – original draft. Dewendra Thakre: methodology, formal analysis, investigation, data curation, and writing – review & editing. Tushar Balasaheb Deshmukh: methodology, formal analysis, investigation, data curation, and writing – review & editing. Sunanda Malo: methodology, formal analysis, investigation, data curation, and writing – review & editing. Subuhan Ahamed: methodology, formal analysis, investigation, data curation, and writing – review & editing. Ravari Kandy Aparna: investigation and data curation. Subham Sahoo: investigation and data curation. Debajit Sarma: conceptualization, writing – review & editing, supervision, and funding acquisition. Kartik Chandra Mondal: conceptualization, writing – review & editing, supervision, and funding acquisition. Babasaheb R. Sankapal: conceptualization, writing – review & editing, supervision, and funding acquisition. Abhishek Banerjee: conceptualization, writing – review & editing, supervision, and funding acquisition.

Conflicts of interest

There are no conflicts to declare.

Acknowledgements

K. S. M. and T. B. D. thank VNIT, Nagpur for providing doctoral fellowship. The authors are grateful to DST-FIST (SR/FIST/CSI-279/2016(C)) for providing the characterization facility. The authors acknowledge SAIF IIT Patna, Prof. Dieter Fenske and the Karlsruhe Nano Micro Facility (KNMF), part of the Helmholtz research infrastructure at the Karlsruhe Institute of Technology (KIT), for performing the single crystal X-ray diffraction measurements.

References

1 T. M. Gür, *Energy Environ. Sci.*, 2018, **11**, 2696–2767.
2 C. Liu, F. Li, L. P. Ma and H. M. Cheng, *Adv. Mater.*, 2010, **22**, E28–E62.
3 C. H. Ng, H. N. Lim, S. Hayase, Z. Zainal, S. Shafie, H. W. Lee and N. M. Huang, *ACS Appl. Energy Mater.*, 2018, **1**, 692–699.
4 D. P. Dubal, O. Ayyad, V. Ruiz and P. Gomez-Romero, *Chem. Soc. Rev.*, 2015, **44**, 1777–1790.
5 M. Winter and R. J. Brodd, *Chem. Rev.*, 2004, **104**, 4245–4270.
6 A. González, E. Goikolea, J. A. Barrena and R. Mysyk, *Renewable Sustainable Energy Rev.*, 2016, **58**, 1189–1206.
7 T. K. Shivasharma, R. Sahu, M. Rath, S. J. Keny and B. R. Sankapal, *J. Chem. Eng.*, 2023, 147191.
8 P. Naskar, A. Maiti, P. Chakraborty, D. Kundu, B. Biswas and A. Banerjee, *J. Mater. Chem. A*, 2021, **9**, 1970–2017.
9 N. S. Choi, Z. Chen, S. A. Freunberger, X. Ji, Y. K. Sun, K. Amine, G. Yushin, L. F. Nazar, J. Cho and P. G. Bruce, *Angew. Chem., Int. Ed. Engl.*, 2012, **51**, 9994–10024.
10 S. Jha, M. Yen, Y. Salinas, E. Palmer, J. Villafuerte and H. Liang, *J. Mater. Chem. A*, 2023, **11**, 3904–3936.
11 Y. Dong, Y. Ma, Y. Li, M. Niu, J. Yang, X. Song, D. Li, Y. Liu and J. Zhang, *Nanoscale*, 2019, **11**, 21180–21187.

12 Z. Zhu, T. Jiang, M. Ali, Y. Meng, Y. Jin, Y. Cui and W. Chen, *Chem. Rev.*, 2022, **122**, 16610–16751.

13 W. Zuo, R. Li, C. Zhou, Y. Li, J. Xia and J. Liu, *Adv. Sci.*, 2017, **4**, 1600539.

14 D. P. Dubal, N. R. Chodankar, D.-H. Kim and P. Gomez-Romero, *Chem. Soc. Rev.*, 2018, **47**, 2065–2129.

15 A. Dutta, S. Mitra, M. Basak and T. Banerjee, *Energy Storage*, 2023, **5**, e339.

16 A. G. Olabi, Q. Abbas, A. Al Makky and M. A. Abdelkareem, *Energy*, 2022, **248**, 123617.

17 M. Salanne, B. Rotenberg, K. Naoi, K. Kaneko, P.-L. Taberna, C. P. Grey, B. Dunn and P. Simon, *Nat. Energy*, 2016, **1**, 1–10.

18 R. R. Salunkhe, Y. H. Lee, K. H. Chang, J. M. Li, P. Simon, J. Tang, N. L. Torad, C. C. Hu and Y. Yamauchi, *Chem.–Eur. J.*, 2014, **20**, 13838–13852.

19 Y. Shao, M. F. El-Kady, J. Sun, Y. Li, Q. Zhang, M. Zhu, H. Wang, B. Dunn and R. B. Kaner, *Chem. Rev.*, 2018, **118**, 9233–9280.

20 A. Patra, K. Namsheer, J. R. Jose, S. Sahoo, B. Chakraborty and C. S. Rout, *J. Mater. Chem. A*, 2021, **9**, 25852–25891.

21 J. Chen and P. S. Lee, *Adv. Energy Mater.*, 2021, **11**, 2003311.

22 T. K. Shivasharma, N. Upadhyay, T. B. Deshmukh and B. R. Sankapal, *ACS Omega*, 2023, **8**, 37685–37719.

23 S. Fleischmann, J. B. Mitchell, R. Wang, C. Zhan, D.-e. Jiang, V. Presser and V. Augustyn, *Chem. Rev.*, 2020, **120**, 6738–6782.

24 C. Largeot, C. Portet, J. Chmiola, P.-L. Taberna, Y. Gogotsi and P. Simon, *J. Am. Chem. Soc.*, 2008, **130**, 2730–2731.

25 B. Conway and W. Pell, *J. Solid State Electrochem.*, 2003, **7**, 637–644.

26 D. P. Chatterjee and A. K. Nandi, *J. Mater. Chem. A*, 2021, **9**, 15880–15918.

27 A. Muzaffar, M. B. Ahamed, K. Deshmukh and J. Thirumalai, *Renewable Sustainable Energy Rev.*, 2019, **101**, 123–145.

28 G. C. Zhang, M. Feng, Q. Li, Z. Wang, Z. Fang, Z. Niu, N. Qu, X. Fan, S. Li and J. Gu, *ACS Appl. Mater. Interfaces*, 2022, **14**, 2674–2682.

29 N. R. Chodankar, H. D. Pham, A. K. Nanjundan, J. F. Fernando, K. Jayaramulu, D. Golberg, Y. K. Han and D. P. Dubal, *Small*, 2020, **16**, 2002806.

30 J.-H. Lee, G. Yang, C.-H. Kim, R. L. Mahajan, S.-Y. Lee and S.-J. Park, *Energy Environ. Sci.*, 2022, **15**, 2233–2258.

31 Z. Yu, L. Tetard, L. Zhai and J. Thomas, *Energy Environ. Sci.*, 2015, **8**, 702–730.

32 Y. Jiao, C. Qu, B. Zhao, Z. Liang, H. Chang, S. Kumar, R. Zou, M. Liu and K. S. Walton, *ACS Appl. Energy Mater.*, 2019, **2**, 5029–5038.

33 E. Frackowiak, *Phys. Chem. Chem. Phys.*, 2007, **9**, 1774–1785.

34 K. Leng, F. Zhang, L. Zhang, T. Zhang, Y. Wu, Y. Lu, Y. Huang and Y. Chen, *Nano Res.*, 2013, **6**, 581–592.

35 P. Veerakumar, A. Sangili, S. Manavalan, P. Thanasekaran and K.-C. Lin, *Ind. Eng. Chem. Res.*, 2020, **59**, 6347–6374.

36 K. Allado, M. Liu, A. Jayapalan, D. Arvapalli, K. Nowlin and J. Wei, *Energy Fuels*, 2021, **35**, 8396–8405.

37 S. Biswas, V. Sharma, D. Mandal, A. Chowdhury, M. Chakravarty, S. Priya, C. C. Gowda, P. De, I. Singh and A. Chandra, *CrystEngComm*, 2020, **22**, 1633–1644.

38 J. Jiang, Y. Li, J. Liu, X. Huang, C. Yuan and X. W. Lou, *Adv. Mater.*, 2012, **24**, 5166–5180.

39 B. Mendoza-Sánchez, T. Brousse, C. Ramirez-Castro, V. Nicolosi and P. S. Grant, *Electrochim. Acta*, 2013, **91**, 253–260.

40 B. Pandit, D. P. Dubal, P. Gómez-Romero, B. B. Kale and B. R. Sankapal, *Sci. Rep.*, 2017, **7**, 43430.

41 A. Dolbecq, E. Dumas, C. R. Mayer and P. Mialane, *Chem. Rev.*, 2010, **110**, 6009–6048.

42 D. Wang, L. Liu, J. Jiang, L. Chen and J. Zhao, *Nanoscale*, 2020, **12**, 5705–5718.

43 J.-N. Chang, M. Zhang, G.-K. Gao, M. Lu, Y.-R. Wang, C. Jiang, S.-L. Li, Y. Chen and Y.-Q. Lan, *Energy Fuels*, 2020, **34**, 16968–16977.

44 A. Banerjee, F. S. Raad, N. Vankova, B. S. Bassil, T. Heine and U. Kortz, *Inorg. Chem.*, 2011, **50**, 11667–11675.

45 L. Zhang and Z. Chen, *Int. J. Energy Res.*, 2020, **44**, 3316–3346.

46 B. Huang, D.-H. Yang and B.-H. Han, *J. Mater. Chem. A*, 2020, **8**, 4593–4628.

47 M. R. Horn, A. Singh, S. Alomari, S. Goberna-Ferrón, R. Benages-Vilau, N. Chodankar, N. Motta, K. K. Ostrikov, J. MacLeod and P. Sonar, *Energy Environ. Sci.*, 2021, **14**, 1652–1700.

48 A. A. Vannathan, T. Kella, D. Shee and S. S. Mal, *Ionics*, 2023, **29**, 4227–4241.

49 V. Ruiz, J. Suárez-Guevara and P. Gomez-Romero, *Electrochem. Commun.*, 2012, **24**, 35–38.

50 J. Madhusree, P. R. Chandewar, D. Shee and S. S. Mal, *RSC Adv.*, 2023, **13**, 26744–26754.

51 K.-p. Wang, K. Yu, J.-h. Lv, M.-l. Zhang, F.-x. Meng and B. Zhou, *Inorg. Chem.*, 2019, **58**, 7947–7957.

52 Y. Hou, H. Pang, C. J. Gomez-Garcia, H. Ma, X. Wang and L. Tan, *Inorg. Chem.*, 2019, **58**, 16028–16039.

53 S. A. Alshehri, A. Al-Yasari, F. Marken and J. Fielden, *Macromol*, 2020, **53**, 11120–11129.

54 Y. Ji, L. Huang, J. Hu, C. Streb and Y.-F. Song, *Energy Environ. Sci.*, 2015, **8**, 776–789.

55 T. Li, P. He, Y. n. Dong, W. Chen, T. Wang, J. Gong and W. Chen, *Eur. J. Inorg. Chem.*, 2021, **2021**, 2063–2069.

56 D. Thakre, A. Anandan Vannathan, A. Banerjee and S. S. Mal, *Ionics*, 2022, **28**, 4001–4010.

57 A. A. Vannathan, D. Thakre, S. R. Ali, M. De, A. Banerjee and S. S. Mal, *J. Solid State Chem.*, 2021, **304**, 122566.

58 D. Thakre, S. R. Ali, S. Mehta, N. Alam, M. Ibrahim, D. Sarma, A. Mondal, M. De and A. Banerjee, *Cryst. Growth Des.*, 2021, **21**, 4285–4298.

59 J. Koziskova, F. Hahn, J. Richter and J. Kozisek, *Acta Chim. Slov.*, 2016, **9**, 136–140.

60 G. M. Sheldrick, *Acta Crystallogr.*, 2008, **64**, 112–122.

61 A. Dolbecq, L. Lisnard, P. Mialane, J. Marrot, M. Bénard, M.-M. Rohmer and F. Sécheresse, *Inorg. Chem.*, 2006, **45**, 5898–5910.

62 D. V. Srinivasa Rao, R. Dandala, G. K. Narayanan, R. Lenin, M. Sivakumaran and A. Naidu, *Synth. Commun.*, 2007, **37**, 4359–4365.
63 B. Pandit, S. A. Pande and B. R. Sankapal, *Chin. J. Chem.*, 2019, **37**, 1279–1286.
64 D. Thakre, Ethylidene Pyridine Bisphosphonate based Polyoxometalates Synthesis Structure and Properties, PhD thesis, Visvesvaraya National Institute of Technology, 2022, **http://hdl.handle.net/10603/441989**.
65 L. Schwiedrzik, V. Brieskorn and L. Gonzalez, *ACS Catal.*, 2021, **11**, 13320–13329.
66 H. Tan, W. Chen, D. Liu, Y. Li and E. Wang, *Dalton Trans.*, 2010, **39**, 1245–1249.
67 X. Sun, R. Ban, P. Ma, J. Wang, D. Zhang, J. Niu and J. Wang, *Synth. Met.*, 2017, **223**, 19–25.
68 A. Saad, G. Rousseau, H. El Moll, O. Oms, P. Mialane, J. Marrot, L. Parent, I.-M. Mbomekallé, R. Dessapt and A. Dolbecq, *J. Cluster Sci.*, 2014, **25**, 795–809.
69 A. Saad, W. Zhu, G. Rousseau, P. Mialane, J. Marrot, M. Haouas, F. Taulelle, R. Dessapt, H. Serier-Brault and E. Rivière, *Chem.–Eur. J.*, 2015, **21**, 10537–10547.
70 A. Boulmier, X. Feng, O. Oms, P. Mialane, E. Rivière, C. J. Shin, J. Yao, T. Kubo, T. Furuta and E. Oldfield, *Inorg. Chem.*, 2017, **56**, 7558–7565.
71 R. Freitag and J. Conradie, *J. Chem. Educ.*, 2013, **90**, 1692–1696.
72 P. L. Tregenna-Piggott, *Inorg. Chem.*, 2008, **47**, 448–453.
73 L. Yang, Z. Zhou, P. Ma, J. Wang and J. Niu, *Cryst. Growth Des.*, 2013, **13**, 2540–2547.
74 D. Kumar, S. Ahmad, G. V. Prakash, K. V. Ramanujachary and A. Ramanan, *CrystEngComm*, 2014, **16**, 7097–7105.
75 N. Maheswari and G. Muralidharan, *Appl. Surf. Sci.*, 2017, **416**, 461–469.
76 T. D. Keene, D. M. D'Alessandro, K. W. Krämer, J. R. Price, D. J. Price, S. Decurtins and C. J. Kepert, *Inorg. Chem.*, 2012, **51**, 9192–9199.
77 R. Ban, Y. Liang, P. Ma, D. Zhang, J. Niu and J. Wang, *Inorg. Chem. Commun.*, 2016, **71**, 65–67.
78 M. Roy, S. Ghosh and M. K. Naskar, *Mater. Chem. Phys.*, 2015, **159**, 101–106.
79 C. Madi, M. Tabbal, T. Christidis, S. Isber, B. Nsouli and K. Zahraman, *J. Phys.: Conf. Ser.*, 2007, **59**, 600.
80 K. M. Racik, K. Guruprasad, M. Mahendiran, J. Madhavan, T. Maiyalagan and M. V. A. Raj, *J. Mater. Sci.: Mater. Electron.*, 2019, **30**, 5222–5232.
81 J. G. Choi and L. T. Thompson, *Appl. Surf. Sci.*, 1996, **93**, 143–149.
82 M. C. Biesinger, L. W. M. Lau, A. R. Gerson and R. S. C. Smart, *Appl. Surf. Sci.*, 2010, **257**, 887–898.
83 G. Silversmit, D. Depla, H. Poelman, G. B. Marin and R. De Gryse, *J. Electron Spectrosc. Relat. Phenom.*, 2004, **135**, 167–175.
84 K. Idczak and R. Idczak, *Metall. Mater. Trans. A*, 2020, **51**, 3076–3089.
85 D. Liu, J. Diao, Y. Qiu, G. Wang, G. Li and B. Xie, *High Temp. Mater. Process.*, 2020, **39**, 351–356.
86 M. Fujiwara, T. Matsushita and S. Ikeda, *J. Electron Spectrosc. Relat. Phenom.*, 1995, **74**, 201–206.
87 J. Telser, C.-C. Wu, K.-Y. Chen, H.-F. Hsu, D. Smirnov, A. Ozarowski and J. Krzystek, *J. Inorg. Biochem.*, 2009, **103**, 487–495.
88 P. L. Tregenna-Piggott, H. Weihe, J. Bendix, A.-L. Barra and H.-U. Güdel, *Inorg. Chem.*, 1999, **38**, 5928–5929.
89 J. Krzystek, A. Ozarowski, J. Telser and D. C. Crans, *Coord. Chem. Rev.*, 2015, **301–302**, 123–133.
90 J. Krzystek, G. J. Yeagle, J.-H. Park, R. D. Britt, M. W. Meisel, L.-C. Brunel and J. Telser, *Inorg. Chem.*, 2003, **42**, 4610–4618.
91 S. S. Khutsishvili, G. N. Chernysheva and I. B. Rozentsveig, *Struct. Chem.*, 2020, **31**, 1793–1800.
92 N. Domracheva, I. Ovchinnikov, A. Turanov, G. Lattermann and A. Facher, *Phys. Solid State*, 2001, **43**, 1188–1194.
93 S. Stoll and A. Schweiger, *J. Magn. Reson.*, 2006, **178**, 42–55.
94 I. A. Kühne, A. Ozarowski, A. Sultan, K. Esien, A. B. Carter, P. Wix, A. Casey, M. Heerah-Booluck, T. D. Keene and H. Müller-Bunz, *Inorg. Chem.*, 2022, **61**, 3458–3471.
95 M. Retegan, M.-N. Collomb, F. Neese and C. Duboc, *Phys. Chem. Chem. Phys.*, 2013, **15**, 223–234.
96 P. Zabierowski, J. Szklarzewicz, R. Gryboś, B. Modryl and W. Nitek, *Dalton Trans.*, 2014, **43**, 17044–17053.
97 M. A. Hassan, F. Ahmad and Z. M. Abd El-Fattah, *J. Alloys Compd.*, 2018, **750**, 320–327.
98 S. Liu, J. Du, Z. Song, C. Ma and Q. Liu, *Light: Sci. Appl.*, 2023, **12**, 181.
99 R. E. Schreiber, H. Cohen, G. Leitus, S. G. Wolf, A. Zhou, L. Que Jr and R. Neumann, *J. Am. Chem. Soc.*, 2015, **137**, 8738–8748.
100 B. R. Sankapal, H. B. Gajare, S. S. Karade and D. P. Dubal, *RSC Adv.*, 2015, **5**, 48426–48432.
101 S. S. Raut, B. R. Sankapal, M. S. A. Hossain, S. Pradhan, R. R. Salunkhe and Y. Yamauchi, *Eur. J. Inorg. Chem.*, 2018, **2018**, 137–142.
102 Y. Gu, D. Xu, S. Chen, F. You, C. Hu, H. Huang and J. Chen, *ACS Omega*, 2022, **7**, 48320–48331.
103 H. K. Rathore, M. Hariram, M. K. Ganesha, A. K. Singh, D. Das, M. Kumar, K. Awasthi and D. Sarkar, *J. Colloid Interface Sci.*, 2022, **621**, 110–118.
104 X. Lu, M. Yu, T. Zhai, G. Wang, S. Xie, T. Liu, C. Liang, Y. Tong and Y. Li, *Nano Lett.*, 2013, **13**, 2628–2633.
105 H. Qin, S. Liang, L. Chen, Y. Li, Z. Luo and S. Chen, *Sustainable Energy Fuels*, 2020, **4**, 4902–4933.
106 T. B. Deshmukh, P. Babar and B. R. Sankapal, *Energy Fuels*, 2023, **37**, 11406–11418.